Abstracts

from session C

Pore radius distribution and fractal dimension derived from spectral induced polarization

Zeyu Zhang
Southwest Petroleum University
Institute of Earth Science and Technology,
Xindu Str. 8, 610500 Chengdu, China
zeyuzhangchina@163.com

Andreas Weller
Institut für Geophysik, TU Clausthal
Arnold-Sommerfeld-Str.1,
38678 Clausthal-Zellerfeld, Germany
andreas.weller@tu-clausthal.de

SUMMARY

The pore radius distribution provides a suitable description of the pore space geometry that can be used to investigate the fractal nature of the pore space or to determine a fractal dimension. Fractal dimension describes the size of geometric objects as a function of resolution. It can be integrated into models of permeability predicting.
We investigated the fractal dimension of the pore space of 24 Eocene sandstone samples from China. We propose an approach to use induced polarization spectra to determine the fractal dimension of the pore space. Debye decomposition was used to determine the relaxation time distribution from the spectra The relaxation time was transferred into a curve showing the cumulative volume intensity as a function of pore radius. The slope of this curve in double logarithmic presentation indicates the fractal dimension. Additionally, the fractal dimension was derived from data of the capillary pressure curves from mercury intrusion and the transversal relaxation time distribution of nuclear magnetic resonance. The results were compared and discussed. For samples with an effective pore radius larger than one micrometer, good agreements exist between the values of fractal dimension derived from the three different methods.

Key words: pore radius, fractal dimension, nuclear magnetic resonance, mercury intrusion capillary pressure, spectral induced polarization.

INTRODUCTION

The distribution of relaxation times of spectral induced polarization (SIP) seems to be controlled by the distribution of the pore sizes. Many studies investigated the relationship between the relaxation time of SIP and the pore/grain geometry. Lesmes and Morgan (2001) developed a model to invert dielectric spectra for effective grain size distributions. Binley et al. (2005) indicated that the mean relaxation time of induced polarization is a measure of a characteristic hydraulic length scale and also the dominant pore throat size. Kruschwitz et al. (2010) examined the low frequency electrical spectra of a range of natural and artificial porous media and observed a power law relationship between the relaxation time and the dominant pore diameter for a subset of their samples. Titov et al. (2010) discovered a positive logarithmic relationship between the relaxation time and the pore throat diameter. Revil et al. (2012) compared the relationship between the induced polarization relaxation time of clean sands and sandstones with both the grain size and the pore size. Current mechanistic models (Revil et al., 2014) assume a relation between relaxation time and pore radius.
Our study demonstrates the use of SIP to determine the fractal dimension of the pore space. It compares the fractal dimension and pore size distribution with the results of nuclear magnetic resonance (NMR) and mercury intrusion capillary pressure method (MICP).

METHODS AND RESULTS

We transformed the relaxation time distribution of complex conductivity spectra determined by Debye decomposition (Nordsiek and Weller, 2008) into a curve showing the cumulative intensity as a function of increasing pore radius r calculated from relaxation time τ. We adopt an equation proposed by Schwarz (1962) and applied by Revil et al. (2012) for the Stern layer polarization model:

$$r = \sqrt{2\tau D_{(+)}} \qquad (1)$$

with $D_{(+)}$ being the diffusion coefficient of the counter-ions in the Stern layer. Originally, this equation describes the relation between the radius of spherical particles in an electrolyte solution and the resulting relaxation time. Though it is questionable whether the radius of spherical grains can be simply replaced by the pore radius, we follow this approach. Additionally, we assume a constant diffusion coefficient $D_{(+)} = 3.8\times10^{-12}$ m²/s as proposed for clayey material (Revil, 2013).
The total chargeability is attributed to the total pore volume. The volume fraction $V_c = V(<r)/V$ is the cumulative volume fraction of pores with radii less than r, which corresponds to the ratio of cumulative intensity to total intensity.
This approach was applied to 24 rock samples from an Eocene sandstone formation in China (Zhang and Weller, 2014). The cumulative curve is presented in a double logarithmic plot showing the relation $\log(V_c)$ versus $\log(r)$. Figure 1 displays this curve for sample CS-5. In the case of fractal behaviour of the pore volume distribution, the slope s of the fitting line is used to get the fractal dimension $D_{IP} = 3 - s$. The resulting fractal dimension D_{SIP} varies for the investigated samples in a range between 2.507 to 2.761.
The red line in Figure 1 marks the effective hydraulic radius, which has been determined from permeability k and formation factor F:

$$r_{eff} = \sqrt{8Fk}\ . \qquad (2)$$

Figure 2 displays the comparison of the pore radii determined at $V_c = 0.5$ from three different methods NMR, MICP and SIP.

The agreements between r_{eff} and r_{50} are different for the applied methods. MICP provides a good agreement between r_{eff} and r_{50}. The radius r_{50} determined by NMR indicates a slight underestimation of the effective pore radius. The radius r_{50} resulting from SIP shows for samples with r_{eff} < 1 µm a strong overestimation.

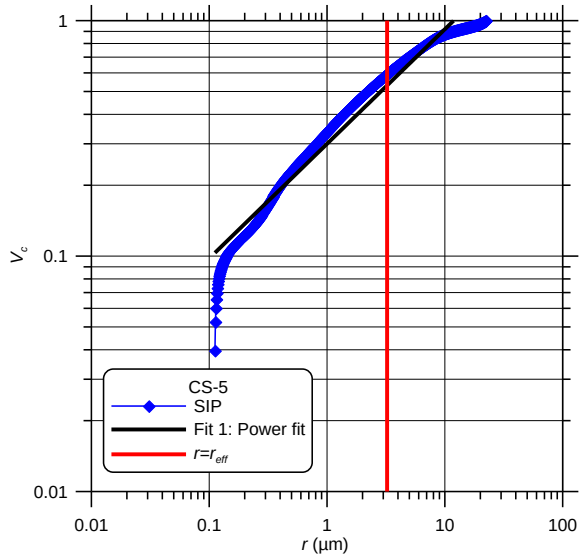

Figure 1. The fractal dimension D_{SIP} of sample CS-5 is determined from the slope of the linear fitting equation $\log(V_c) = 0.487 \log(r) - 1.205$ ($R^2 = 0.967$) with $D_{SIP} = 3 - 0.487 = 2.513$. The vertical red line indicates $r = r_{eff} = 3.24$ µm.

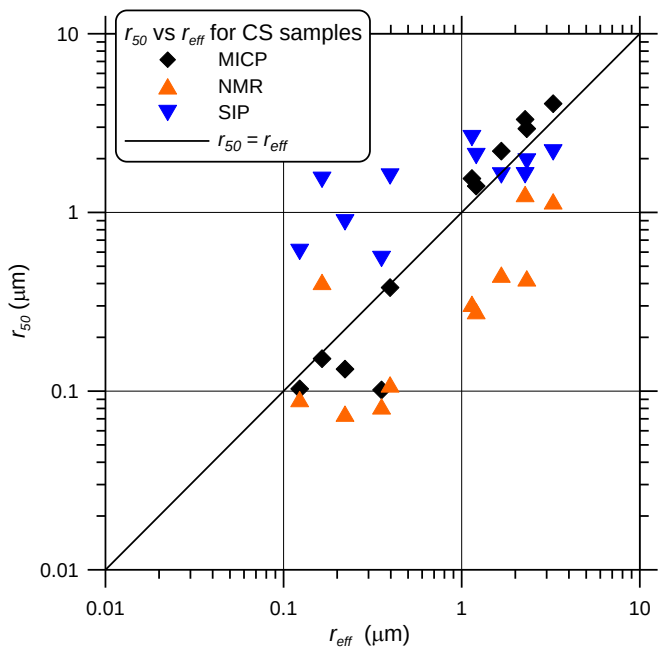

Figure 2: Relation between r_{eff} and r_{50} for 11 sandstone samples. The diagonal line indicates $r_{eff} = r_{50}$.

The samples with a wide permeability range of 0.02 to 60 mD were subdivided into three classes with high (H-samples), medium (M-samples), and low permeability (L-samples). The L-samples indicate either a strong compaction or a rich sedimentation of carbonates in the pore space that results in low porosity and small pore radii. The higher permeability of H-samples is caused by low clay and carbonate content and a good sorting.

For H-samples, the V_c-r curves of the methods NMR, MICP and SIP show similar characteristics. The best agreement exists for CS-18 with all cumulative pore radii curves showing the steepest slope close to r_{eff} as shown in Figure 3.

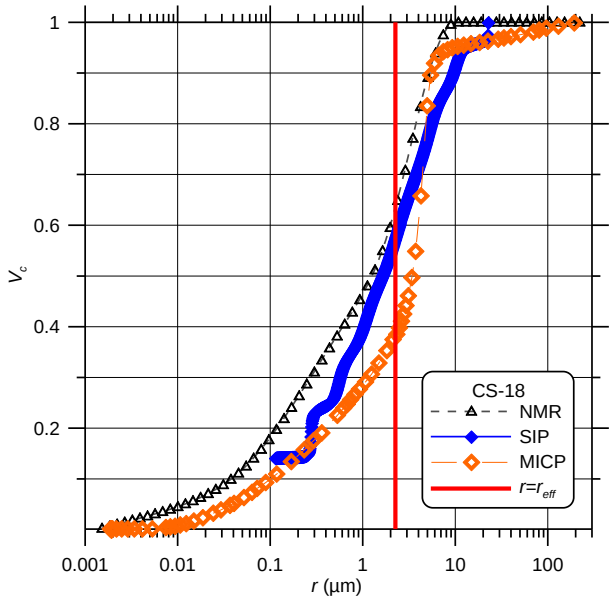

Figure 3: The comparison of V_c-r curves determined from NMR, MICP, and SIP for sample CS-18 (H-sample). The vertical red line indicates $r = r_{eff} = 2.25$ µm.

The M-samples show a good agreement between MICP and SIP, but we observe $r_{NMR} < r_{MICP}$ and a good agreement between NMR and MICP in the lower and upper part of the curves but strong deviation in the middle part. For L-samples there is good agreement between MICP and NMR with r_{eff} close to r_{50}. However, the SIP-curves appear at a much higher r-range. Sample CS-1 is shown as an example in Figure 4. The agreement between the curves can be improved if the constant diffusion coefficient used in equation 1 is replaced by a lower value $D_{(+)} = 0.38\times10^{-12}$ m²/s that corresponds to the apparent diffusion coefficient. It is determined using r_{eff} and τ_{peak} that results from the frequency of the maximum of the imaginary part of conductivity σ"(f) (Weller et al., 2016).

If a constant diffusion coefficient is used all V_c–r curves are displayed in the same range of pore radii covering only two orders of magnitude (0.1 to 20 µm). It should be noted that the V_c-r-curves of MICP and NMR cover four orders of magnitude. The reason for this phenomenon is the restricted frequency range (2 mHz to 100 Hz) of the used spectra. The frequency range f > 100 Hz is not regarded because of electromagnetic coupling effects. The resulting restricted r-range is caused by the relation $r \sim f^{-0.5}$. Higher frequencies with f > 100 Hz would be necessary to get information on lower radii from SIP.

Figure 5 displays the comparison between the fractal dimension D_{SIP} with the fractal dimension derived from MICP and NMR. In order to enable an unbiased comparison, the same r-range of 0.1 to 10 µm was applied for all methods. The fractal dimension derived from NMR and MICP are close to

each other, and are higher than the calculated fractal dimension determined from SIP.

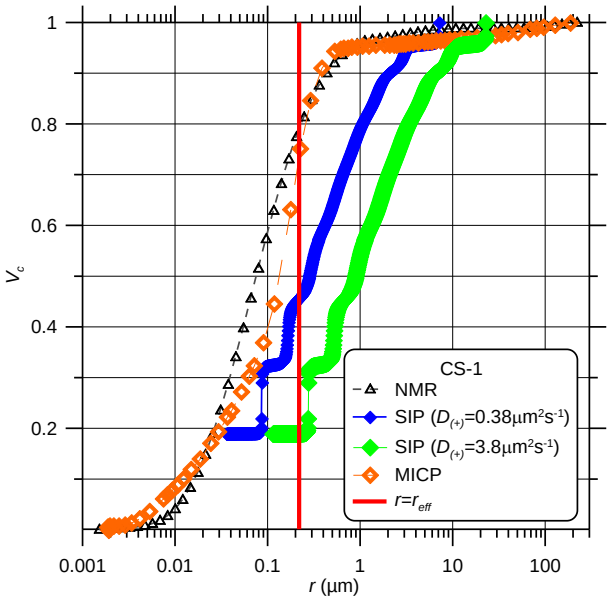

Figure 4: The comparison of V_c-r curves determined from NMR, MICP and SIP methods for sample CS-1 (L-sample). Additionally, the apparent diffusion coefficient $D_{(+)}$ = 0.38×10^{-12} m²/s is used. The vertical red line indicates r = r_{eff} = 0.22 µm.

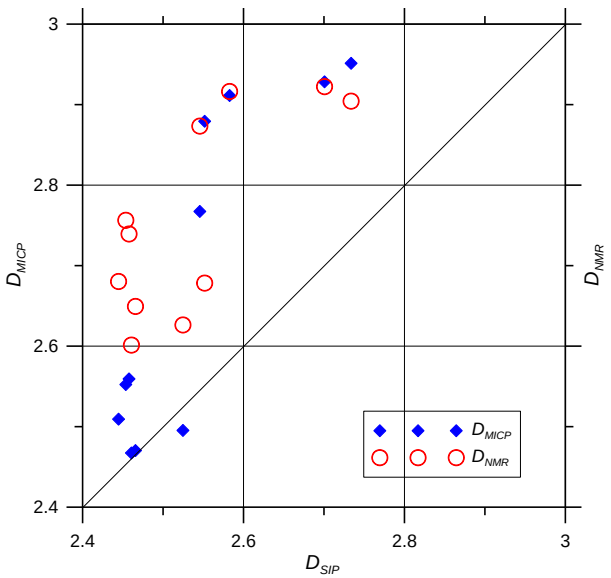

Figure 5: The comparison of fractal dimensions determined from NMR, MICP and SIP methods. The diagonal line indicates D_{SIP} = D_{NMR} = D_{MICP}.

Figure 6 displays the comparison between the effective pore radius r_{eff} and the fractal dimension derived from NMR, MICP and SIP methods. The fractal dimension decreases with the increasing effective pore radius.

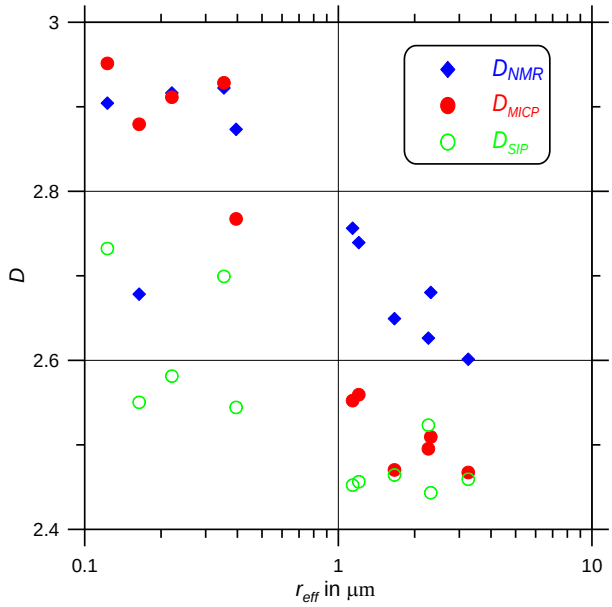

Figure 6: The comparison of effective pore radius and fractal dimension determined from NMR, MICP and SIP methods.

CONCLUSIONS

The study has shown that a fractal dimension can be determined on the basis of an IP relaxation time distribution. If we use a constant diffusion coefficient a good agreement can be observed with the V_c–r curves of MICP and NMR for samples with r_{eff} > 1 µm. Samples with smaller pore radii indicate larger deviations in the resulting V_c-r curves. This problem can be overcome if instead of a constant diffusion coefficient the apparent diffusion coefficient is used.
Further investigations will demonstrate the integration of fractal dimension in models of permeability prediction.

ACKNOWLEDGMENTS

The authors thank Sabine Kruschwitz, Wolfgang Debschütz, Matthias Halisch, and Sven Nordsiek for supporting the measurements and data processing of this study.

REFERENCES

Binley, A., Slater, L. D., Fukes, M., and Cassiani G., 2005, Relationship between spectral induced polarization and hydraulic properties of saturated and unsaturated sandstone: Water Resources Research, 41, W12417, doi:10.1029/2005WR004202.

Kruschwitz, S. F., Binley, A., Lesmes, D., and Elshenawy, A., 2010, Textural controls on low-frequency electrical spectra of porous media: Geophysics, 75, 4, WA113–WA123.

Lesmes, D. P., and Morgan, F. D., 2001, Dielectric spectroscopy of sedimentary rocks: Journal of Geophysical Research: Solid Earth, 106, 13329 –13346, doi: 10.1029/2000JB900402.

Nordsiek, S., and Weller, A., 2008, A new approach to fitting induced-polarization spectra: Geophysics, 73, No. 6, F235-F245, doi: 10.1190/1.2987412.

Revil, A., Koch, K. and Holliger, K., 2012, Is it the grain size or the characteristic pore size that controls the induced polarization relaxation time of clean sands and sandstones?: Water Resources Research, 48, W05602, doi:10.1029/2011WR011561.

Revil, A., 2013, Effective conductivity and permittivity of unsaturated porous materials in the frequency range 1 mHz-1GHz: Water Resources Research, 49, 306-327, doi: 10.1029/2012WR012700.

Revil, A., Florsch, N., and Camerlynck, C. 2014, Spectral induced polarization porosimetry: Geophysical Journal International, 198, 1016-1033, doi: 10.1093/gji/ggu180.

Schwarz, G., 1962, A theory of the low-frequency dielectric dispersion of colloidal particles in electrolyte solution: Journal of Physical Chemistry, 66, 2636-2642, doi: 10.1021/j100818a067.

Titov, K., Tarasov, A., Ilyin, Y., Seleznev, N., and Boyd, A., 2010, Relationships between induced polarization relaxation time and hydraulic properties of sandstone: Geophysical Journal International, 180, 1095–1106. doi:10.1111/j.1365246X.2009.04465.x.

Weller, A., Zhang, Z., Slater, L., Kruschwitz, S., and Halisch, M., 2016, Induced polarization and pore radius - a discussion: 4th International Workshop on Induced Polarization, Aarhus.

Zhang, Z., and Weller, A. 2014, Fractal dimension of pore-space geometry of an Eocene sandstone formation: Geophysics, 79, No. 6, D377-D387. doi: 10.1190/geo2014-0143.1.

2D DCR/TDIP Two-step Inversion: Detectability of ore deposits and Depth of Investigation

Juliane Adrian
Institute of Geophysics and Meteorology,
University of Cologne
Albertus-Magnus-Platz, 50923 Cologne, Germany
adrian@geo.uni-koeln.de

Bülent Tezkan
Institute of Geophysics and Meteorology,
University of Cologne
Albertus-Magnus-Platz, 50923 Cologne, Germany
tezkan@geo.uni-koeln.de

SUMMARY

The joint application of the Direct Current Resistivity (DCR) and Time-domain Induced Polarization (TDIP) methods is a helpful tool to investigate ore deposits with sulfidic content. The combined interpretation yields a resistivity and chargeability model of the subsurface which is superior to a pure resistivity model, especially when dealing with disseminated deposits.
We present a newly developed smoothness constrained 2D inversion algorithm for DCR and TDIP data applying a two-step approach. It contains a Finite Element forward calculation on an unstructured triangular mesh which amongst others simplifies the incorporation of topography.
The new algorithm is tested regarding the quality of the chargeability resolution with respect to the resistivity model. Furthermore, the resolution of the lower boundary of a highly chargeable model block is investigated and compared to the depth of investigation which is determined by the coverage matrix.
Finally, 2D inversion results of field data acquired on a sulfidic copper ore deposit in Turkey are shown using the newly developed algorithm and a feasible interpretation is given.

Key words: Direct Current Resistivity, Time-domain, Induced Polarization, Inversion, Ore Exploration

INTRODUCTION

Ore deposits often appear as disseminated sulfidic materials. Exploring these deposits with the DCR method alone is challenging because the resistivity signature caused by disseminated material is often hard to detect. The TDIP method, on the other hand, is qualified to detect areas with disseminated sulfidic ores due to large electrode polarization effects resulting in large chargeability anomalies. By employing both methods we gain information about both, the resistivity and the chargeability distribution of the subsurface.

Here, we present the current state of the development of a 2D smoothness constraint inversion algorithm for DCR and TDIP data. The implemented forward algorithm uses a Finite Element approach with an unstructured mesh. The model parameters resistivity ρ and chargeability m are connected by a conductivity perturbation approach after Seigel (1959):

$$\rho_{IP}=\rho_{DC}/(1-m) \ .$$

That means the presence of material with chargeability m>0 increases the intrinsic resistivity ρ_{DC} to the effective resistivity ρ_{IP}. The calculation of synthetic apparent chargeability m_a is realized by double DC forward calculation (Seigel, 1959):

$$m_a=\frac{f_{DC}(\rho_{IP})-f_{DC}(\rho_{DC})}{f_{DC}(\rho_{IP})} \ .$$

The smoothness constrained inversion is a common inversion approach in applied geophysics and was e.g. realized by Sasaki (1994) or Günther *et al.* (2006). Here, the following normal equation is solved with respect to the model update Δm:

$$\left(J^T W_d^T W_d J+\lambda C^T C\right)\Delta m=J^T W_d^T W_d \Delta d$$

with the error weighting matrix W_d, the data misfit Δd and the lagrange parameter λ which regulates the tradeoff between model roughness and data fitting. The Jacobian matrix J is determined according to the superposition method which saves computational time. The smoothness constrained matrix C takes into account the size and shape of the triangular elements of the unstructured mesh.
The determination of a resistivity and a chargeability model is realized by a two-step inversion approach following Oldenburg and Li (1994): At first, a pure DCR inversion is carried out yielding in a resistivity model. This model is kept fixed and is used as a basis for the forward calculation of apparent chargeability values within the chargeability inversion.

The new developed algorithm is tested by the inversion of synthetic data. The result of the first modeling study is that the resolution of a highly chargeable model block seems to be rather independent of the corresponding resistivity anomaly; at least if the chargeability contrast is high enough. The second modeling study deals with the sensitivity and depth of investigation. It is investigated in which depth the lower boundary of a highly chargeable block can be resolved with a given multi-electrode setup. It is found that the coverage matrix V is a helpful tool to determine the resolution depth. The entries of V are

$$v_j=\frac{1}{v_{max}}\sum_{i=1}^{N}|W_{d,ii}J_{ij}|$$

for N data points and j=1,...,M elements.

Finally, 2D inversion results of DCR/TDIP field data acquired on a sulfidic copper ore deposit in Turkey are shown. The results show highly chargeable areas which clearly suggest the presence of a copper ore content below 8 m depth.

MODELING SYNTHETIC DATA

All modeling studies were calculated for the same multi-electrode setup that was used in the survey in 2013: pole-dipole configuration, profile length 300 m, distance between consecutive electrodes 10 m and 20 m.

Chargeability Resolution

The first modeling study with synthetic data investigates if a highly chargeable model block can be resolved by the inversion and whether the resolution of this block is dependent on the corresponding resistivity structure or not. First, synthetic pole-dipole data (apparent resistivity and apparent chargeability) was calculated for a model block with 100 mV/V within a homogeneous halfspace with 10 mV/V (see Figure 1a). Three different resistivity models were used with resistivity of the block of 80 Ωm, 100 Ωm and 150 Ωm. The resistivity of the surrounding homogeneous halfspace is 100 Ωm. Then, an inversion was carried out with the different synthetic datasets using the same initial model which is a homogeneous halfspace regarding resistivity and chargeability. The chargeability inversion result of all three synthetic datasets is shown in Figure 1b-d. The shape and the amplitude of the anomaly is similar to each other, independent from the corresponding resistivity model.

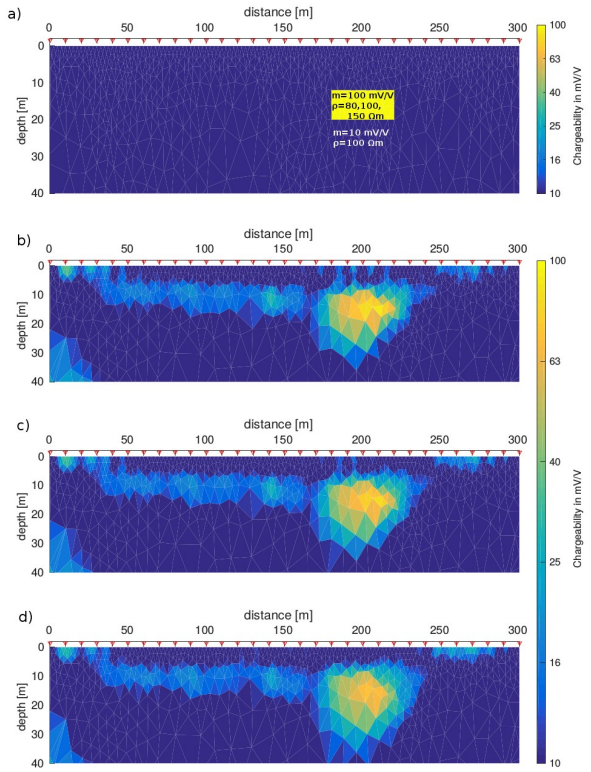

Figure 1. a) Original chargeability and resistivity model used to calculate three synthetic pole-dipole datasets (each with apparent chargeability and apparent resistivity). The chargeability model is the same for all three datasets, whereas the resistivity of the model block is varied. b-d) Chargeability inversion results for synthetic datasets calculated from the model in a): Original resistivity of the model block b) 80 Ωm, c) 100 Ωm and d) 150 Ωm. Electrode positions are indicated by red triangles.

Depth Resolution

In order to investigate the chargeability resolution with depth a modeling study with synthetic pole-dipole data calculated from chargeability models consisting of a chargeable model block (100 mV/V) with different depth of the the lower boundary within a homogeneous halfspace of 10 mV/V was

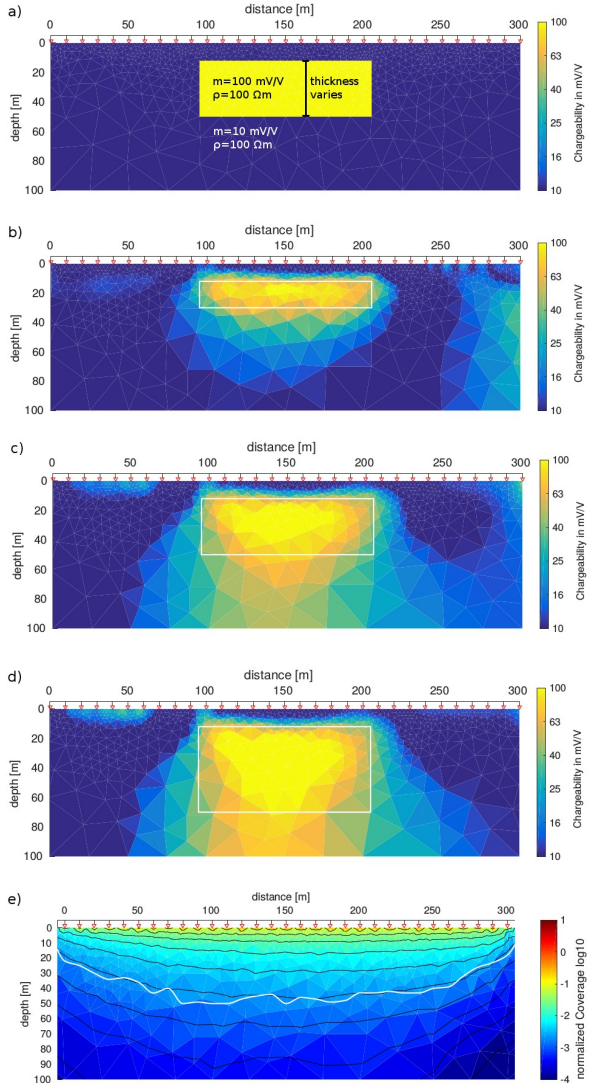

Figure 2. a) Original chargeability and resistivity model used to calculate different synthetic pole-dipole datasets (each with apparent chargeability and apparent resistivity). The thickness of the model block is varied. b-d) Chargeability inversion results for synthetic datasets calculated from the model in a): lower boundary of the model block b) 30 m, c) 50 m, d) 70 m. The original extension of the model blocks is indicated by a white rectangle. Electrode positions are indicated by red triangles. e) Coverage normalized to element size calculated from the Jacobian of the chargeability model in d). The white line indicates the contour line of the coverage threshold.

carried out (see Figure 2a). The lower boundary varies between 20 m depth and 100 m. The corresponding resistivity model is a homogeneous halfspace with 100 Ωm. The electrode distance does not increase when modeling larger thickness because we want to estimate the resolution in depth for a fixed electrode setup and derive a measure for it. Some chargeability inversion results of the synthetic data are shown in figure 2b-d. The lower boundary of the highly chargeable block is resolved until a depth of ca. 70 m. However, the depth of investigation (doi) after the rule of thump (which is a third of the largest distance between the current electrode and the second potential electrode) is only

53 m below the surface. To find a measure for the depth resolution or sensitivity, which is more detailed, we can use the normalized coverage (see Figure 2e). A resolution threshold might be derived from the coverage values calculated for a homogeneous halfspace (initial model) in a certain depth in the center of the profile. This depth might e.g. correspond to the doi after the rule of thumb which was used to find the coverage threshold (white line) in Figure 2e. However, there still seems to be sufficient resolution below this line, thus it is still to be investigated how to choose a more reliable coverage threshold.

INVERSION OF FIELD DATA

In 2013 a field survey was carried out on a disseminated copper ore deposit in Elbistan, Turkey. Pole-dipole DCR/TDIP data was acquired on 8 profiles (see Figure 3) perpendicular to the assumed strike direction of the ore deposit. The lateral extension of the deposit is assumed to decrease from profile 1 to profile 8. The resistivity and chargeability inversion results for profile 1 are shown in Figure 4 left. Most prominent in the resistivity result is a conducting area close to the surface in the center of the profile which is dipping to the right. This might correspond to sediments underlying an agricultural field in this location. The resistivity is higher in the beginning and end of the profile which is assumed to correspond to mineralized rocks that were cropping out at the end of the profile. Below the conducting area in the center, the resistivity is slightly higher. This result fits to the inversion results of RMT data, acquired on the same profiles.

The chargeability result shows low chargeability values close to the surface and the chargeability is increased below ca. 8 m depth, reaching more than 100 mV/V. This clearly suggests the presence of the expected sulfidic copper. Unfortunately, the lateral extension and the lower boundary of this deposit were not resolved with the used multi-electrode setup. However, the chargeability result of e.g. profile 7 (see Figure 4 right) shows a chargeability anomaly that is restricted in lateral direction as was expected.

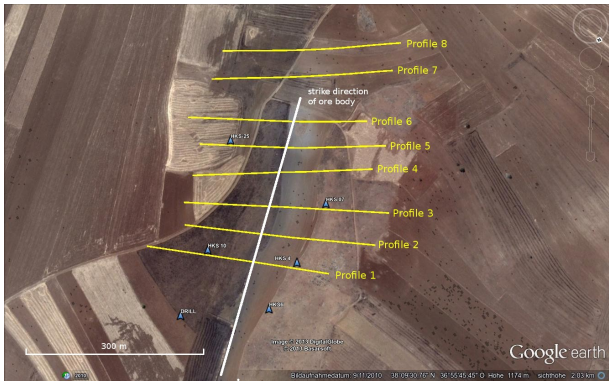

Figure 3. Survey area in Elbistan, Turkey. DCR, TDIP and Radiomagnetotelluric data was acquired on 8 profiles. The assumed strike direction of the copper ore deposit is indicated by a white line, borehole locations by blue triangles.

CONCLUSIONS

A new smoothness constrained 2D DCR/TDIP two-step inversion algorithm using the finite element approach with an unstructured mesh was developed and was tested successfully on synthetic and field data. A modeling study with synthetic data reveals that the resolution of the chargeability model is not necessarily dependent of the corresponding resistivity model. That means that a highly chargeable model block is reconstructed by the resulting chargeability inversion model irrespective of whether the same model block shows a resistivity anomaly or not. Another modeling study suggests the coverage matrix as a helpful tool to determine the depth resolution with respect to the depth of investigation.

The field data inversion results reveal a highly chargeable area below 8 m depth in the center of profile 1 which clearly suggests the presence of an increased sulfidic copper ore content. This assumption is supported by borehole data. Unfortunately, the lower boundary of the deposit is not resolved by the applied geophysical methods. On the other hand, the comparison of the resulting chargeability models of the different profiles shows that the lateral extension of the ore deposit decreases from profile 1 to profile 7. The advantage of a joint application of the DCR and the TDIP method when exploring disseminated deposits is supported by the comparison between the chargeability and the corresponding resistivity models: the extend of the chargeability anomaly does not directly correspond to a resistivity anomaly. This is because the resistivity anomaly caused by disseminated metallic material is rather small and hard to detect.

ACKNOWLEDGMENTS

We thank M. Emin Candansayar and his working group at the Department of Geophysical Engineering, University of Ankara, Turkey for the advice and for the realization of the field campaign.

REFERENCES

Günther, T., Rücker, C., and Spitzer, K., 2006, Three-dimensional modelling and inversion of dc resistivitydata incorporating topography – II. Inversion: Geophysical Journal International, 166, 506-517.

Oldenburg, D. W., and Li, Y., 1994, Inversion of induced polarization data: Geophysics, 59, 1327-1341.

Sasaki, Y., 1994, 3-D resistivity inversion using the finite-element method: Geophysics, 59, 1839-1848.

Seigel, H. O., 1959, Mathematical formulation and type curves for induced polarization: Geophysics, 3, 547-565.

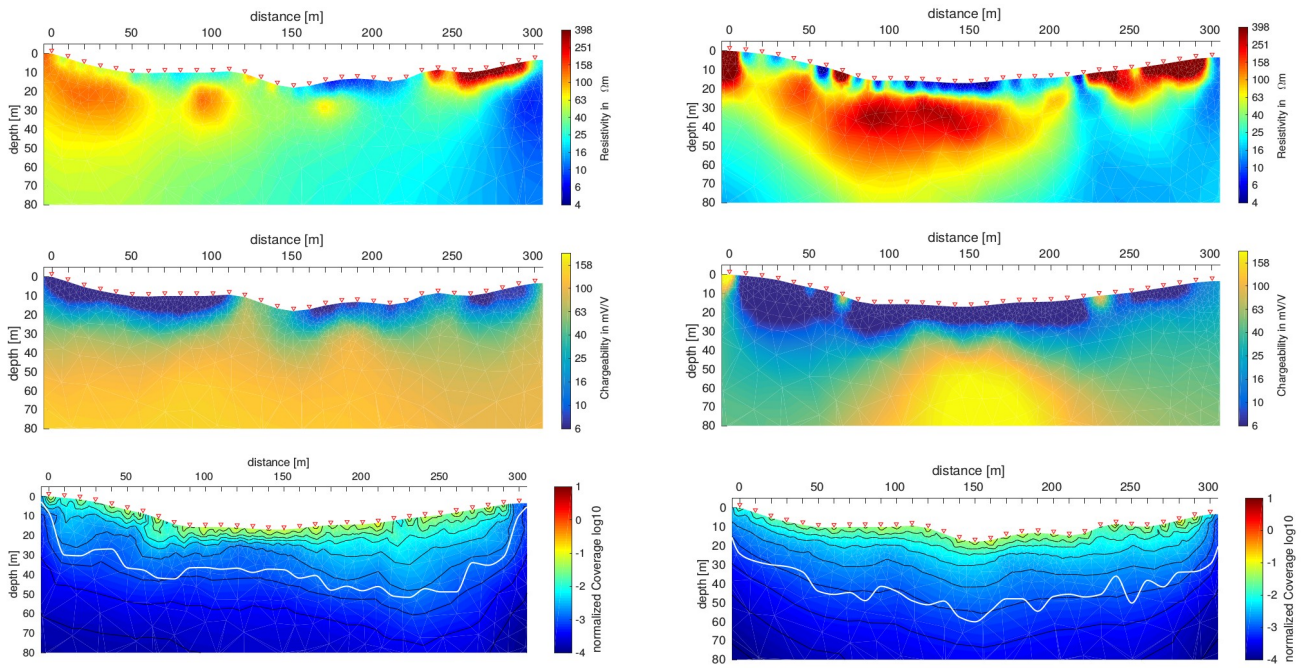

Figure 4. Pole-dipole field data inversion results for profile 1 (left column) and profile 7 (right column). Topography is included. Resistivity model (top), chargeability model (center) and coverage normalized to triangular element size (bottom). The white line indicates the contour line of the coverage threshold. Electrode positions are indicated by red triangles.

IP2016 / 4th International Workshop on Induced Polarization

Large Scale IP Survey at Önneslöv in Southern Sweden

Torleif Dahlin
Engineering Geology, Lund University
Box 118, SE-221 00 Lund, Sweden
torleif.dahlin@tg.lth.se

Per-Ivar Olsson
Engineering Geology, Lund University
Box 118, SE-221 00 Lund, Sweden
per-ivar.olsson@tg.lth.se

Matteo Rossi
Engineering Geology, Lund University
Box 118, SE-221 00 Lund, Sweden
matteo.rossi@tg.lth.se

SUMMARY

A DCIP survey, i.e. a geoelectrical survey with combined measurement of DC resistivity and induced polarization (IP), was conducted in southern Sweden. The purpose was to identify soil depth and bedrock structures and variations in rock quality.

Data were acquired data with 100% waveform from which IP of good quality data were extracted. The inverted model sections show a wide variation in the electrical properties of the bedrock that are expected to relate to variation in rock quality. The results, together with results of other geophysical methods, form the basis for a drilling program in order to identify variations in quality rock of importance to the construction of an underground facility.

Key words: DCIP, time-domain IP, 100% waveform, rock quality.

INTRODUCTION

A DC resistivity and time-domain induced polarisation (DCIP) survey was carried out along four lines at Önneslöv close to Dalby in southern Sweden. The purpose of the survey was to map variations in rock quality as part of site investigations for a planned underground facility. Seismic surveying was made along three of the lines during the same week as the DCIP survey. Magnetic profiling has also been made in the area.

Unstable rock and water bearing rock are common problems in underground construction, and in addition small thickness of rock cover above the facility can created stability problems. Electrical Resistivity Tomography (ERT) has proved to be a useful tool for mapping variations in rock quality that can be linked to variation in rock quality with relevance for underground construction (e.g. Rønning et al 2014; Danielsen and Dahlin 2009; Dahlin et al. 1999), and in this study we aim at refining the characterisation by adding information from the IP effects.

METHOD

Data acquisition was made along 4 lines of 800 – 1000 m length, with three parallel and one perpendicular line (Figure 1). A double cable spread with in total 162 electrodes at 5 m separation was used resulting in an 810 m long layout. The layout with separated electrode cable spreads was employed in order to ensure as good quality data as possible for the IP data by reducing the risk of capacitive coupling in the cables (Dahlin and Leroux 2012) and. A complicating factor for the data acquisition was that a major road with heavy traffic was crossed by three of the lines, which was handled by drilling horizontal boreholes under the road, in which extension cables were used to link together the spread on each side of the road (Figure 1).

Data were measured with an ABEM Terrameter LS with 12 measuring channels using multiple gradient array (Dahlin and Zhou 2006). Data were recorded using a 100% duty cycle waveform (Olsson et al 2015) and 4 s long transmitted pulses.

DCIP data were extracted from the full waveform recordings, saved with a data rate of 3750 Hz, employing a data filtering and processing procedure presented by Olsson et al (2016). For the inversion presented here the IP data were saved as integral apparent chargeabilities.

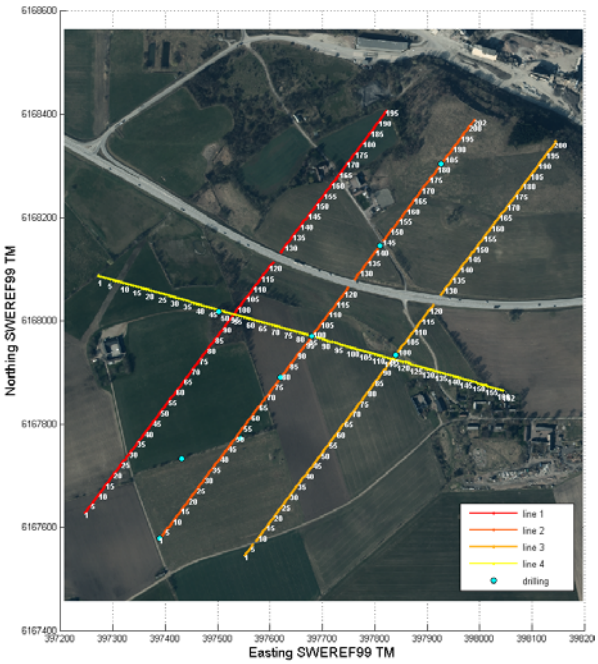

Figure 1. Layout of survey lines in relation to road and quarry.

The contact resistances varied from some hundred Ω to more than 10 kΩ, with mean resistances between 2.2 – 3.8 kΩ. The measured sections contain between 3298 and 4264 data points each, where the number varies depending on the length of the line and the number of electrodes that were excluded in connection with the road crossings. Although power supply harmonic noise and spikes, presumably from electrical cattle

fences, are seen in the full waveform recordings integrated resistivity and chargeability data are of good quality. Hence only 2 - 8 data points were rejected from each of the data sections before inversion.

Res2dinvx64 (ver. 4.04.35) was employed for inverting the data using L1 norm (robust) inversion. Inversion resulted in models with good model fit, with mean residuals in the range 1.1 – 2.8% for resistivity and 1.5 – 4.1% for chargeability.

A large quarry is located immediately north of the investigated area (visible in upper edge of Figure 1) which gives an excellent overview of the geological conditions that can be expected, and an example is shown in Figure 2. After the DCIP and seismic surveys a number of representative points for drilling were pointed out, and in total eight percussion boreholes were drilled to a depth of 200 – 250 m. Geophysical logging is underway for some of the boreholes at the moment of writing.

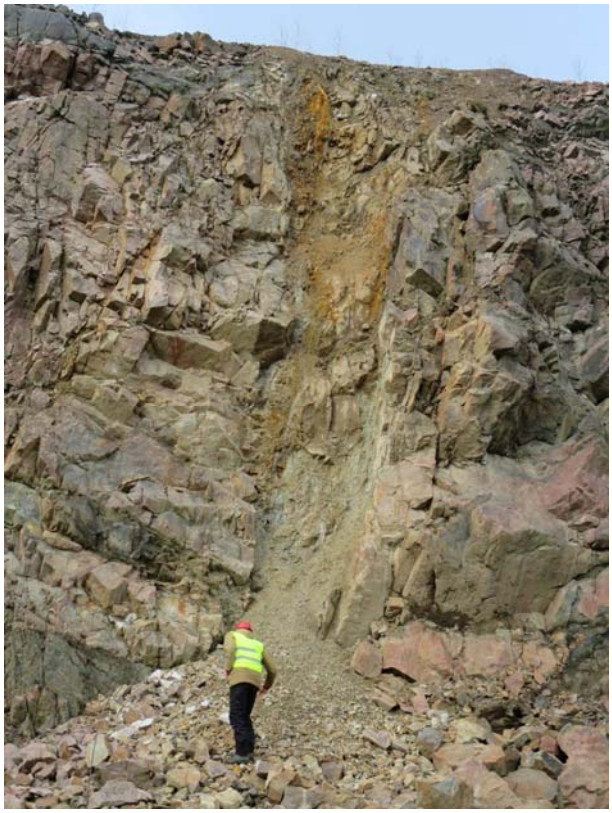

Figure 1. Example of a vertical weathered zone in the quarry which is situated next to the survey area. Notice the highly fractured character of the rock mass surrounding the zone, it is typical for the rock that is exposed in the quarry.

RESULTS

The resistivity models (Figure 3a and Figure 4a) show a top layer with lower resistivity with mostly less than 10 m thickness, but in some places there is up to 20-30 m thickness (e.g. Line 1-400 m; Line 3-550 m). This top low resistivity layer is interpreted as soil, which is verified by the drilling (Figure 4). In some places where the underlying structures have low resistivity, there is no clear boundary between the upper and lower layers, e.g. Line 2 at 700 m (Figure 4a). In parts of the area a thin layer with higher resistivity on top of the low-resistivity upper layer can be seen.

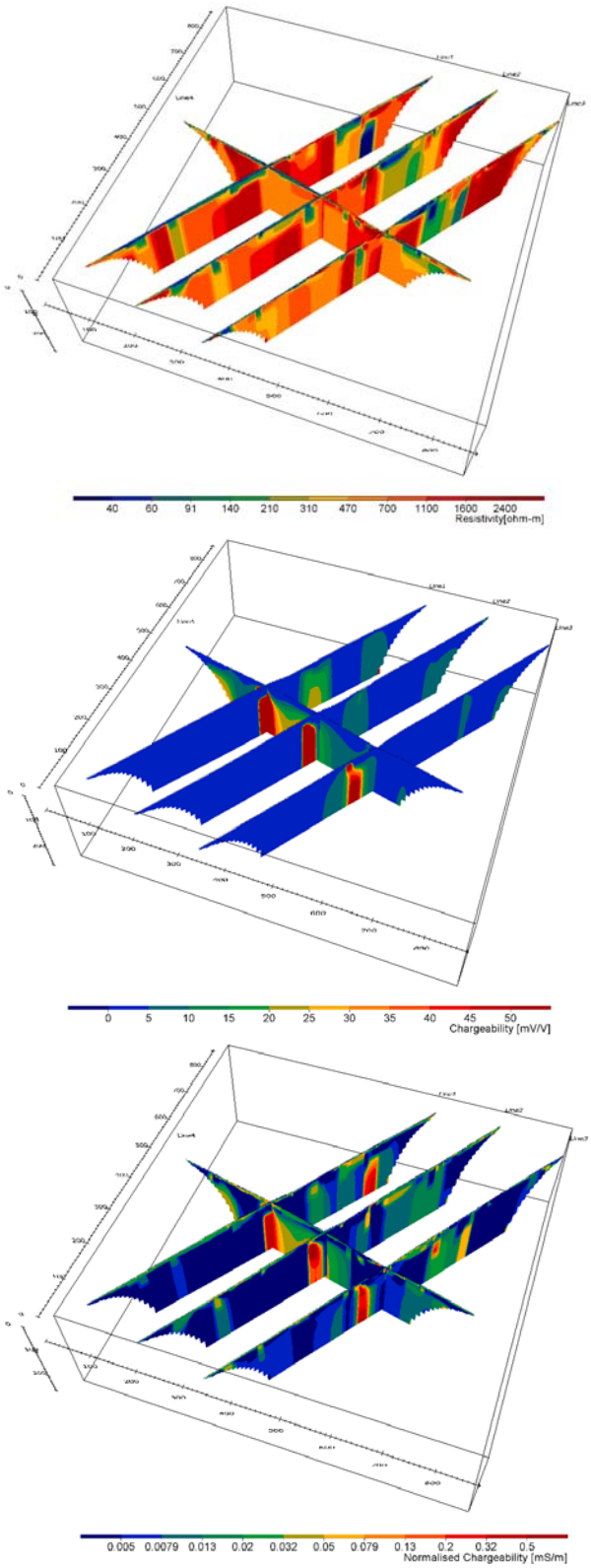

Figure 3. Overview of inverted models from Önneslöv; a) resistivity, b) chargeability, c) normalised chargeability.

The resistivity sections (Figure 3a and Figure 4a) are otherwise dominated by a number of more or less vertical structures with alternating low and high resistivity. The resistivity of these zones vary from under 40 to over 2400 Ωm, with large zones with resistivities of a few hundred Ωm. This is interpreted as bedrock with varying degrees of fracturing and weathering, where the bedrock consists of gneiss, amphibolite and dolerite dykes and minor elements of other rocks. The most highly resistive parts are expected to be composed of rock with a relatively low fracture density, while lower resistivities suggest higher degree of fracturing and possible weathering. The most low-resistive zones are expected to be associated with the most weathered parts of the rock, which may be associated with stability problems during underground construction. Crystalline rock with resistivity in the range of hundreds Ωm can be interpreted as water bearing, where potentially high hydraulic conductivity that can provide rock engineering problems.

IP models for the three parallel lines (Figure 3b and Figure 4b) are similar in that all exhibit a sharp and distinct anomaly with a high chargeability close to the centre of the section (>100 mV/V). This zone is also visible in the shorter perpendicular line but with a more extended appearance, as one might expect since the zone is crossed with a different angle to the line. Furthermore, there are more diffuse zones with increased chargeability in the north-eastern part of the three parallel lines. The most distinct zone coincides with a zone of lower resistivity. The zone can be interpreted as rock with a high degree of fracturing and weathering, and mineralization, e.g. a fractured and weathered dolerite dyke. Because the zone is below or close to a telephone cable which is no longer used, it cannot be completely ruled out that it is caused by it, but the depth the top of the anomaly above the edge and their extent at depth to the contrary. The more diffuse zones with elevated chargeability can be caused by tectonised and fractured rock, with mineralization and weathering.

The normalized chargeability (Figure 3c and Figure 4c) shows basically the same as the previous, but some nuances emerge more clearly. For example, a transition that could constitute the transition between soil and fractured rock emerges in parts of sections.

CONCLUSIONS AND OUTLOOK

The DCIP survey shows a top layer that is reflecting depth to bedrock and a wide variation in the electrical properties of the bedrock that appear to reflect the variation in rock quality which is expected at Önneslöv judging from the nearby quarry. Data will be inverted for spectral IP parameters, and an in-depth analysis of the DCIP models along with documentation from drilling, sampling and analysis will be done with the aim to characterize the rock in terms of variation in the properties of relevance to underground construction. The information obtained from the available percussion drilling is however limiting the possibilities to find correlation between the drilling documentation and the geoelectrical models. Geophysical borehole logging is done as complement to feedback detailed results from borehole measurements to DCIP model sections, to allow for more detailed analyses and more extensive interpretation. The borehole measurements include flow log, natural gamma radiation, sonic and resistivity-IP.

ACKNOWLEDGMENTS

Funding for the work was provided by Skanska Sverige AB, Formas - The Swedish Research Council for Environment, Agricultural Sciences and Spatial Planning, (ref. 2012-1931), BeFo - Swedish Rock Engineering Research Foundation, (ref. 314 and 331) and SBUF - The Development Fund of the Swedish Construction Industry, (ref. 12718 and 12719). The project is part of the Geoinfra-TRUST framework (Transparent Underground Structure, http://www.trust-geoinfra.se/). We thank Skanska Sverige AB and Sweco Environment AB for a fruitful cooperation.

REFERENCES

Dahlin T. and Leroux V., 2012, Improvement in time-domain induced polarisation data quality with multi-electrode systems by separating current and potential cables: Near Surface Geophysics, 10, 545-565.

Danielsen, B.E. and Dahlin, T., 2009, Comparison of geoelectrical imaging and tunnel documentation. Engineering Geology, 107, 118–129.

Dahlin, T. and Zhou, B., 2006, Multiple-gradient array measurements for multichannel 2D resistivity imaging: Near Surface Geophysics, 4, 113-123.

Dahlin, T., Bjelm, L. and Svensson, C., 1999, Use of electrical imaging in site investigations for a railway tunnel through the Hallandsås Horst, Sweden, Quarterly Journal of Engineering Geology, 32(2), 163-173.

Olsson P.-I., Dahlin T., Fiandaca G. and Auken E., 2015, Measuring time domain spectral induced polarization in the on-time – decreasing the acquisition time and increasing the signal levels: Journal of Applied Geophysics, 123, 316-321.

Olsson P.-I., Fiandaca G., Juul Larsen J., Dahlin T. and Auken E., 2016, Doubling the spectrum of time-domain induced polarization by harmonic de-noising, drift correction, spike removal, tapered gating and data uncertainty estimation, Geophysical Journal International, submitted manuscript.

Rønning J.S., Ganerød G.V., Dalsegg E., Reiser F., 2014, Resistivity mapping as a tool for identification and characterisation of weakness zones in crystalline bedrock: definition and testing of an interpretational model, Bull Eng Geol Environ, 73, 1225–1244.

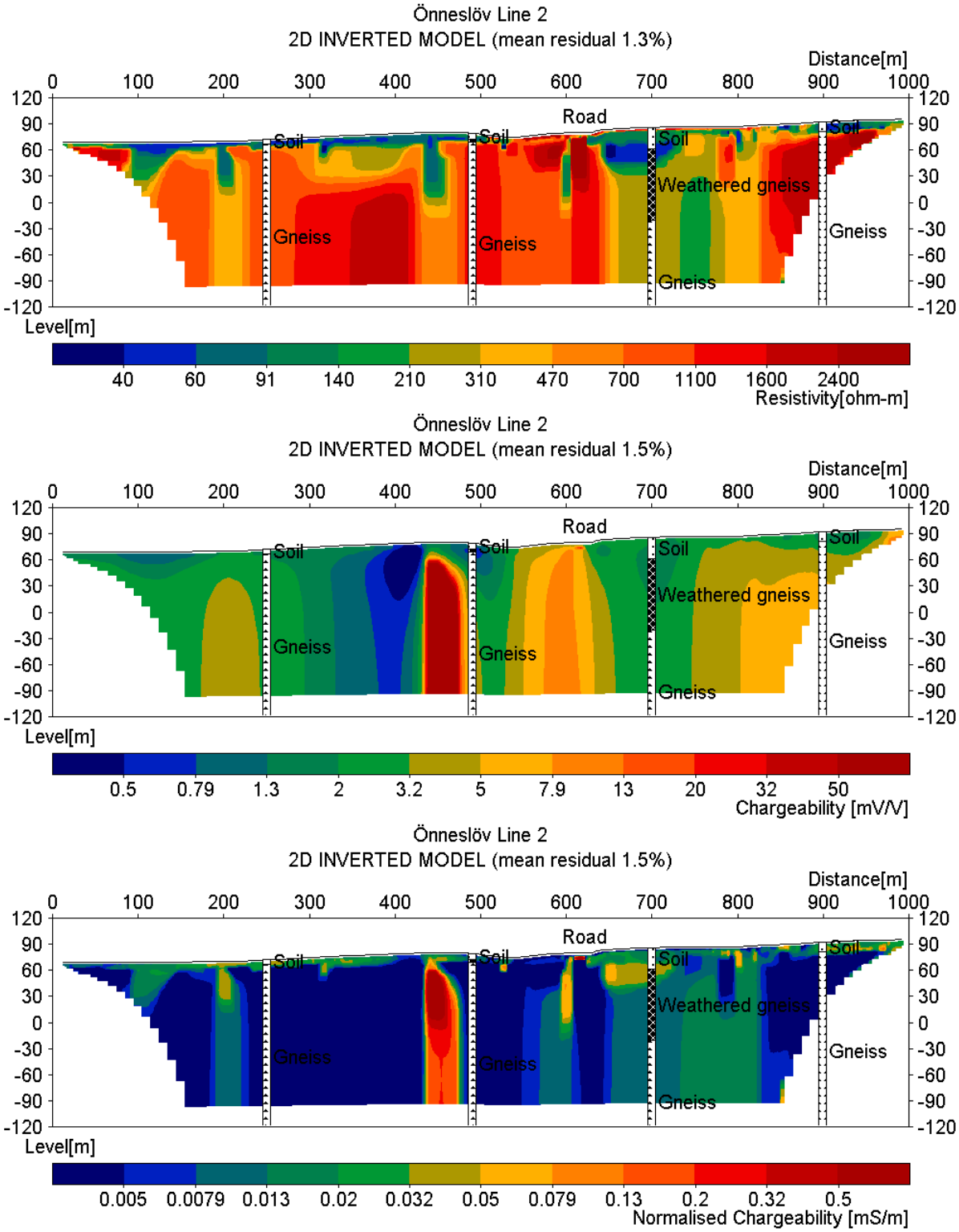

Figure 4. Inverted models from Line 2 at Önneslöv with geological logs from percussion drilling; a) resistivity, b) chargeability, c) normalised chargeability.

An Approach for Microscale Simulation for Induced Polarization

Dr. Norbert Klitzsch
E.ON ERC, RWTH Aachen University
Mathieustrasse 10, 52074, Aachen, Germany
nklitzsch@eonerc.rwth-aachen.de

Saurabh Singh
E.ON ERC, RWTH Aachen University
Mathieustrasse 10, 52074, Aachen, Germany
ssingh@eonerc.rwth-aachen.de

SUMMARY

In this paper, we discuss an approach for the microscopic simulations for Induced Polarization that describes the dynamics of ion transport with the help of the Nernst-Planck-Poisson (NPP) model. The NPP model is governed by coupled diffusion and migration equations. The equations are solved by means of the Finite Difference Method and Euler schemes. The goal is to develop SIP simulation tool that takes the inner 3D microstructure of the porous media into account. So far we have successfully verified and validated the 1D and 2D NPP models. We also introduced time dependent IP simulations on simple 2D models.

Key words: Microscale simulations, Electrical Double Layer, Diffuse Layer, Stern Layer, Nernst-Planck-Poisson equations, Finite Difference Method (FVM), Induced Polarization (IP)

INTRODUCTION

Understanding the SIP response of rocks is still a challenge even though many model approaches were published. For instance, [Revil and Glover, 1998; Leroy and Revil, 2004, Volkmann and Klitzsch, 2010] provide interesting overviews on the numerical and empirical developments in the context of the SIP. However, most of the models describing the induced polarization are based on simplified assumptions regarding both the microstructure and the physics of the processes at the rock-electrolyte interface. Moreover, the simulations of porous medium behaviour often treat the medium as homogeneous in nature and link their material properties to microstructural properties by empirical equations.

Our goal is to develop a superior approach for simulating SIP for porous medium that accounts for the real inner 3D microstructure. Here, we present 1D and 2D time dependant IP simulations.

THEORY

In porous media such as rocks or batteries, the interaction between electrolyte and solid material give rise to a charged solid surface and thus to the so called Electrical Double Layer (EDL) at their interface. The EDL arises in the electrolyte to compensate the charge of the solid surface; it consists of the Stern layer of counter-ions adsorbed to the solid surface and the diffuse layer with increasing concentration differences between cations and anions towards the solid surface. The EDL is the only cause of the IP effect in rocks which do not contain electronic conductors.

We introduce our approach for modeling coupled ion migration and diffusion processes governed by the Nernst-Planck-Poisson (NPP) equations. The NPP equations totally cover the physics of the diffuse layer of the EDL but do not include adsorption effects required for describing the Stern layer. Moreover, the length and time scales needed for modeling the Stern layer are at least 10 times smaller than for modeling the diffuse layer. Molecular dynamics would be required for describing the Stern layer explicitly which we do not intend to utilize.

APPROACH FOR IP SIMULATION

The module developed (in MATLAB®) simulates the coupled diffusion and migration of charges in an electric field which is governed by the NPP equations. As the first step, non-dimensionalization of the NPP model is performed. The non-dimensional PDE system provides better conditioning and is much faster (i.e. lower iteration count) to solve with the iterative numerical solvers. The equations are discretized in space and time using the second order Finite Difference Method (FDM) and the first order Euler schemes.

In the course of the development, we realized that coupled diffusion and migration equations are numerically unstable and requires greater care in terms of numerics. Moreover, the concentration of the electrolyte is one of the crucial parameters because of its influence on the Debye length. The electrolyte concentration thus indirectly influences the domain size of the model which was initially obscure for 2D or 3D simulation. We also examined the role of different boundary conditions on the simulation outcome.

We will briefly present our approach as follows:

Step 1: We simulated the steady state solution for the ionic concentrations and the potential distribution in an electrolyte around a charged solid particle. We imposed no flux boundary conditions for the ions and zero potential boundary condition at the outer boundary of the domain. Moreover, we imposed no flux boundary conditions for the ions and non-zero Neumann condition for the potential around the charged solid particle. We verified the simulation by comparing the numerical result with the analytical solution (1D) (Figure 1).

Step 2: In the next step, we simulated the steady state solution for the model above but applying an external potential across the model domain. For that, we imposed Dirichlet boundary conditions for the ions (i.e. prescribing to the equilibrium

concentration) and for the potential (i.e. prescribing to external voltage) around the model domain. We imposed no flux boundary condition for the ions and non-zero Neumann condition for the potential around the charged solid particle.
Step 3: After a while, the external voltage source is switched off and the behaviours for the ions concentration and potential is observed. All the boundary conditions for the ions and the potential remain the same as taken during the Step 2.

RESULTS

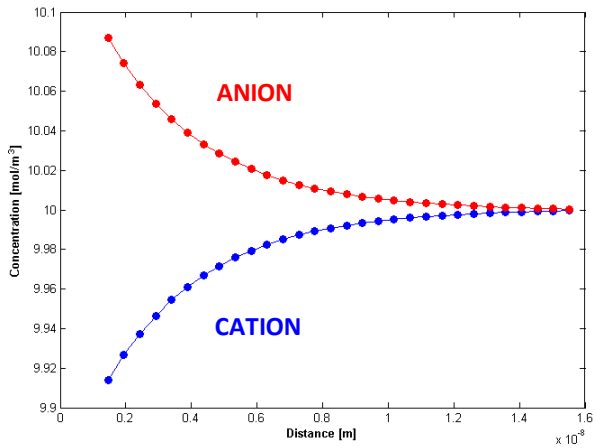

Figure 1: Comparison of the numerical (lines) and the analytical (circles) solution for the 1D NPP model (16 nm domain). It shows the charge separation at the positively charged interface leading to the formation of the Debye layer.

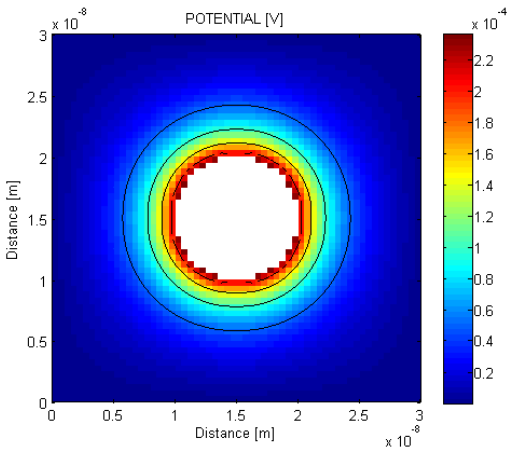

Figure 2: 2D potential distribution of the NPP model around a positively charged particle.

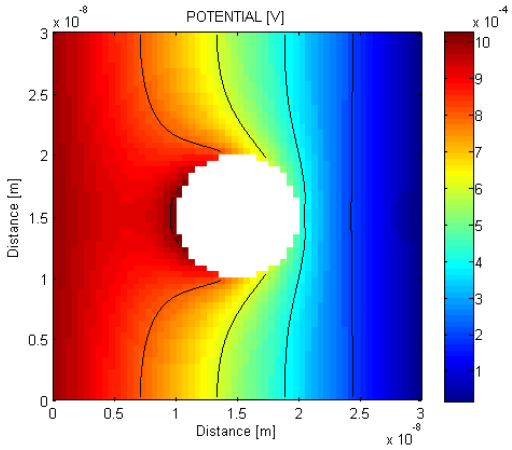

Figure 3: 2D potential distribution with an applied external voltage around a positively charged particle.

CONCLUSIONS

We introduce microscopic simulation of time domain induced polarization with the help of the Nernst-Planck-Poisson (NPP) model. The NPP equations are coupled ion migration and diffusion equations which are discretised in space with the help of the Finite Difference Method and in time with the help of the Euler Schemes.

We will use the model for parameter studies such as influence of particle size and pore size on the IP response. We intend to present the results at the internal IP Workshop at Aarhus.

ACKNOWLEDGMENTS

This work is a part of collaborative research project involving the Institute of Applied Geophysics and Geothermal Energy, the Institute of Power Generation & Storage Systems (both RWTH Aachen University), and the Math2Market GmbH. The project is funded by the gGmbH E.ON Energy Research Center.

REFERENCES

Revil, A., and Glover, P.W.J., 1998, Nature of surface electrical conductivity in natural sands, sandstone, and clay, Geophysical Research Letters, Vol. 25.

Leroy, P., and Revil, A., 2004, A triple-layer model of the surface electrochemical properties of clay minerals, Journal of Colloid and Interface Science, Vol. 270.

Volkmann, J., and Klitzsch, N., 2010. Frequency-Dependent Electric Properties of Microscale Rock Model for Frequencies from One Millihertz to Ten Kilohertz, Vadose Zone J, Vol. 9, 858-870.

IP2016 / 4th International Workshop on Induced Polarization

Non-invasive geophysical monitoring of subsurface biogeochemical processes under redox oscillating conditions

Adrian Mellage
University of Waterloo
Earth & Env. Sciences
200 University Ave. W.
Waterloo, ON. Canada
amellage@uwaterloo.ca

Geertje J. Pronk
University of Waterloo
Earth & Env. Sciences
200 University Ave. W.
Waterloo, ON. Canada
gpronk@uwaterloo.ca

Tatjana Milojevic
University of Waterloo
Earth & Env. Sciences
200 University Ave. W.
Waterloo, ON. Canada
t2miloje@uwaterloo.ca

Anthony L. Endres
University of Waterloo
Earth & Env. Sciences
200 University Ave. W.
Waterloo, ON. Canada
alendres@uwaterloo.ca

Estella A. Atekwana
Oklahoma State University
School of Geology
Stilwater, OK. 74078
United States
estella.atekwana@okstate.edu

Alex Furman
Technion
Civil & Env. Engineering
Haifa 32000
Israel
afurman@technion.ac.il

Fereidoun Rezanezhad
University of Waterloo
Earth & Env. Sciences
200 University Ave. W.
Waterloo, ON. Canada
frezanez@uwaterloo.ca

Philippe Van Cappellen
University of Waterloo
Earth & Env. Sciences
200 University Ave. W.
Waterloo, ON. Canada
pvc@uwaterloo.ca

SUMMARY

In order to determine the effects of water table dynamics on subsurface biogeochemistry, we are currently conducting state-of-the-art automated soil column experiments with fully integrated monitoring of hydro-bio-geophysical variables under both constant and oscillating water table conditions. An artificial, homogeneous mixture consisting of minerals and organic matter is used to provide a well-defined starting material. The artificial soil is packed into 60 cm high, 7.5 cm wide columns. In this experiment, three replicate columns are incubated while keeping the water table constant at mid-depth, while another three columns alternate between drained and saturated conditions. Periodic spectral induced polarization (SIP) measurements are performed, in order to monitor the development of the soil's geophysical signature and relate this to the observed changes in biogeochemical properties. Thus far, during the initial "wetting and drying" cycle of the experiment, the measured imaginary conductivity (σ") response in the fluctuating column shows a decrease during the wetting phase, followed by an increase during the drying phase. Also, the magnitude of σ" increases with decreasing depth, despite the expected lower moisture content closer to the surface. These results are opposite of what would be expected based on the saturation-σ" relationship and have potential implications as to how σ" data are interpreted in variably saturated media. Concurrent measurements of pore-water geochemistry and solid phase microbial analyses will allow us to track changes in soil biogeochemistry and relate these back to the observed complex conductivity response, in order to develop a full theoretical understanding of the processes controlling the observed signals. The experiment is ongoing with an expected total duration of 6 months.

Key words: Spectral induced polarization, imaginary conductivity, complex conductivity, biogeochemistry.

INTRODUCTION

The general lack of data and knowledge on the biogeochemical functioning of the subsurface, under redox oscillating conditions (e.g., water table fluctuations), severely limits our ability to predict the impacts of anthropogenic pressures on soil and groundwater resources. A new, and likely game changing, approach to unraveling subsurface biogeochemical processes and microbial interactions is the application of non-invasive, non-destructive geophysical methods (Atekwana and Atekwana, 2010). A key advantage of geophysical techniques is that they can provide *in situ* information at high spatial and temporal resolution, without the need for intrusive sampling and time consuming (and expensive) *ex situ* analyses.

Spectral induced polarization (SIP) has been shown to be sensitive to the processes mentioned above, and has the potential to be used as a proxy measurement technique to monitor subsurface biogeochemistry at larger spatial and temporal scales. SIP measures the impedance magnitude and phase-shift (φ) between an injected current and the subsequent resultant voltage potential (Abdel Aal and Atekwana, 2014; Schwartz *et al.*, 2014). The SIP measurements are conducted at varying frequencies, typically from 0.01 to 1000 Hz. The measurable decrease in electrical field amplitude and the phase shift arise due to energy dissipation processes and the polarized/charged character of soils (Schwartz *et al.*, 2014). SIP has been shown to be sensitive to microbially driven geochemical processes in soils (Davis *et al.*, 2006; Slater *et al.*, 2007), as well as, abiotic processes, such as: mineral dissolution (Placencia-Gómez *et al.*, 2013); changes in surface area per unit volume (Weller *et al.*, 2010) and changes in the degree of saturation (Ulrich and Slater, 2004).

The main objective of this study is to advance our fundamental understanding of the effects of water table dynamics on the biogeochemical functioning of the subsurface, while assessing geophysical signatures (SIP) as proxies for the monitoring of biogeochemical processes and microbial interactions in the subsurface. This study also allows us to demonstrate and validate the use of SIP in a laboratory setting.

METHODS

The artificial soil is composed of 77.5% quartz sand, 10% montmorillonite, 2.5% goethite and 10% humus from a forested riparian zone, from which we also extracted the microbial inoculum added to the soil mixture. The artificial soils were packed into six columns (60 cm high and 7.5 cm in diameter), to a height of 45 cm. Three of the replicate columns are incubated while keeping the water table constant at mid-depth, while another three columns alternate between drained and saturated conditions (Figure 1). The water table regimes were imposed using a computer-controlled, multi-channel pump connected to a hydrostatic equilibrium reservoir and a water storage reservoir (see Rezanezhad *et al*., 2014 for more details about this soil column setup). The soil columns were saturated by upward flow of artificial groundwater (AGW). The equilibrium and storage columns were sparged continuously with argon gas to ensure anoxic conditions.

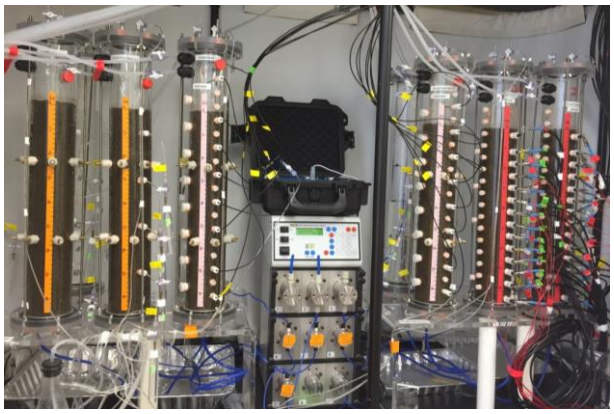

Figure 1. Multi component/interdisciplinary soil column experiment with biogeochemical and geophysical monitoring underconstant (left) and fluctuating (right) water table.

For each of the replicate sets, one column was fitted with Ag-AgCl current coil-electrodes and Ag-AgCl agar-filled potential electrodes (Figure 1). Two current electrodes were inserted at the top and bottom of the soil column and 12 potential electrodes (allowing for 6 SIP measurement pairs) were placed in between, 4 cm from each current electrode, with a 3 cm spacing between each potential electrode. All SIP data were measured using a Portable Spectral Induced Polarization Unit (Ontash & Ermac Inc., NJ, USA).

All columns were fitted for the monitoring of pore-water geochemistry. One column for the drying/wetting and one for the constant water content treatment respectively, was fitted with redox potential electrodes, as well as, oxygen sensors at regular depth intervals. In addition, the headspace above the soil surface is closed for 10 min, every 1-2 days in order to measure the build-up of CO_2 and CH_4, allowing us to derive the gaseous efflux from the soil during the experiment. These measurements will allow us to elucidate the controls behind the measured geophysical responses.

PRELIMINARY RESULTS

So far we have observed periodic redox potential variations during the wetting and drying cycles in the fluctuating water table column. Constant redox potentials, in the order of 600 and -200 mV, were recorded in the constant water table column whereas in the fluctuating water table column, redox potentials at the same depths oscillated between oxidizing (+600 mV) and reducing (-400 mV) conditions. The most pronounced differences in E_h were observed in the mid-section of the fluctuating column (i.e., transition zone). Soil CO_2 emissions (derived from headspace gas analysis) showed variations in the columns due to a combination of gas diffusion dynamics and the onset of aerobic/anaerobic soil respiration. Pulsed CO_2 fluxes were observed at the onset of water table drawdown.

The SIP time-series data have shown a distinct evolution in the imaginary conductivity (σ") response, both at depth and with time. Imaginary conductivity data at 1 Hz, for the potential electrode pairs at the mid-section of the fluctuating water table column, are plotted in Figure 2. The σ" response decreased at all depths during the wetting period and the drop was most pronounced at depths (below the soil surface) of 13.5 cm and 19.5 cm. Following the wetting period, the drying phase resulted in an increase in the σ" at all depths. After 1 week the σ" stabilized at depths of 31.5, 25.5 and 19.5 cm and continued to rise at depth 13.5 cm. It is expected that the trends in the imaginary conductivity signal be highly dependent on the degree of saturation at depth. Imaginary conductivity has been shown to correlate positively with increasing saturation, but can also be a function of saturation range and history (Ulrich and Slater, 2004). In our depth profile measurements the magnitude of the measured σ" increases with decreasing depth, which is opposite to the trend expected based on the imposed hydraulic regime. Also, during the onset of drying we observed an increase in the σ" response, particularly at depths of 13.5 and 19.5 cm. Our hypothesis is that several competing processes, such as, increased microbial activity within the depth profile due to the infiltration of oxygen, as well as, the potential formation of aggregates may contribute to the observed response. A comparison of solid-phase analysis and pore-water geochemistry data will help to elucidate these different processes.

CONCLUSIONS

The preliminary results for the initial "wetting and drying" phase have shown a distinct imaginary conductivity response. The measured imaginary conductivity (σ") response in the fluctuating column shows a decrease during the wetting phase, followed by an increase during the drying phase. The magnitude of σ" increases with decreasing depth – despite the expected lower moisture content closer to the surface. The factors controlling this response are likely biogeochemical in nature. In order to elucidate their contribution to the signal a comparison of the SIP response to concurrent solid-phase analyses and pore water geochemistry data is necessary. We are confident that these data will shed light on the controls behind the observed response.

REFERENCES

Abdel Aal, G.Z. and Atekwana, E.A. 2014. Spectral induced polarization (SIP) response of biodegraded oil in porous media. Geophysical Journal International, 196, 804-817.

Atekwana, E. A., & Atekwana, E. A. 2010. Geophysical signatures of microbial activity at hydrocarbon contaminated sites: a review. Surveys in Geophysics, 31, 247-283.

Atekwana, E. A., & Slater, L. D. 2009. Biogeophysics: A new frontier in Earth science research. Reviews of Geophysics, 47, RG4004.

Davis, C.A., Atekwana, E., Atekwana, E., Slater, L.D., Rossbach, S., Mormile, M. 2006. Microbial growth and biofilm formation in geologic media is detected with complex conductivity measurements. Geophysical Research Letters, 33, LI8403.

Placencia-Gómez, E., Slater, L., Ntarlagiannis, D. and Binley, A., 2013. Laboratory SIP signatures associated with oxidation of disseminated metal sulfides. Journal of Contaminant Hydrology, 148, 25-38.

Rezanezhad, F., Couture, R. M., Kovac, R., O'Connell, D., & Van Cappellen, P. 2014. Water table fluctuations and soil biogeochemistry: An experimental approach using an automated soil column system. Journal of Hydrology, 509, 245-256.

Slater, L., Ntarlagiannis, D., Personna, Y.R. and Hubbard, S., 2007. Pore-scale spectral induced polarization signatures associated with FeS biomineral transformations. Geophysical Research Letters, 34, L21404.

Schwartz, N., Shalem, T., & Furman, A. 2014. The effect of organic acid on the spectral-induced polarization response of soil. Geophysical Journal International, 197, 269-276.

Ulrich, C. and Slater, L., 2004. Induced polarization measurements on unsaturated, unconsolidated sands. Geophysics, 69, 762-771.

Weller, A., Slater, L., Nordsiek, S. and Ntarlagiannis, D., 2010. On the estimation of specific surface per unit pore volume from induced polarization: A robust empirical relation fits multiple data sets. Geophysics, 75, WA105-WA112.

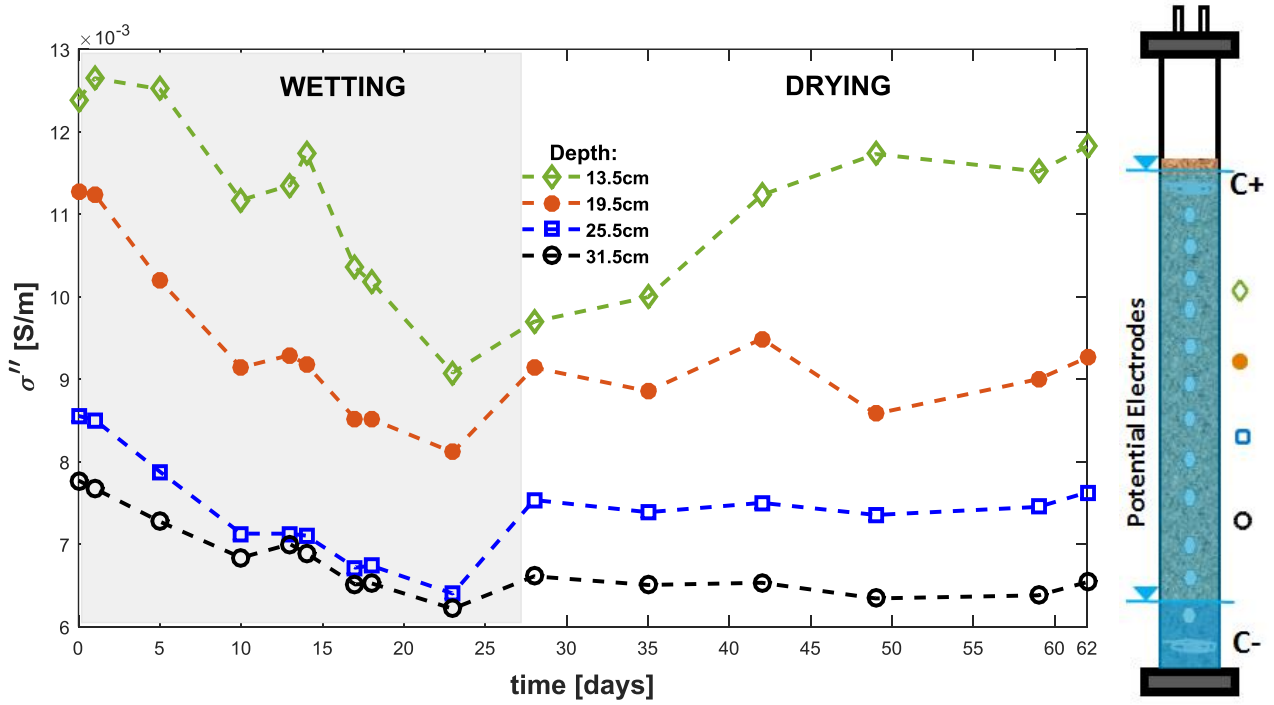

Figure 2. Imaginary conductivity (σ'') data at 1 Hz for the potential electrode pairs at the column mid-section, from the onset of the first wetting period (grey) and the start of the first drying (white) period. The column on the right hand side of the plot denotes the location of the electrode pairs for all plotted data, where C^+ and C^- are the positive and negative current electrodes, respectively.

IP2016 / 4th International Workshop on Induced Polarization

The IP response of black shales in the Oslo graben, Norway

Asgeir Kydland Lysdahl
Norwegian Geotechnical Institute (NGI)
Sognsveien 72, 0855 Oslo, Norway
aol@ngi.no

Erik Endre
Norwegian Geotechnical Institute (NGI)
Sognsveien 72, 0855 Oslo, Norway
eer@ngi.no

Tino Radic
Radic Research
Zehntwerderweg 188A, 13469 Berlin, Germany
tino.radic@t-online.de

Jürgen Scheibz
Norwegian Geotechnical Institute (NGI)
Sognsveien 72, 0855 Oslo, Norway
jus@ngi.no

SUMMARY

This work presents time-domain IP and resistivity field measurements of a black shale lithology in the Oslo graben, as well as a frequency-domain laboratory characterization of the complex impedance of core samples from the same lithology. The time domain inversion models resemble well the known lithology and the black shales stands out with high (40 msec) chargeability. A large phase shift (up to 19 degrees) is recorded in the complex impedance data at low frequencies in two out of three black shale samples. Both results show a significant IP response and suggest the existence of large polarizable aggregates in the black shales.

Key words: Black shales, time-domain IP, frequency-domain IP, geochemistry

INTRODUCTION

Black shales are sedimentary rocks with a particular high content of sulphides and heavy metals. They swell and produce sulfuric acid upon oxidation, they produce radon gas and they have very poor mechanical properties. Black shales are present many places in the Oslo graben, and precise mapping tools are always required.

The different lithological black shales in the Oslo graben have been formed under different anaerobic conditions. Less oxygen present under sedimentation yields in general a higher content of sulphides (comprises mainly pyrite and pyrrhotite) and heavy metals, and the grain size of anaerobic sedimented shales is in general larger. The resulting variety of black shales in Norway are classified by their acidification potential (AP/NP), their Fe/S ratio and furthermore a series of triangular diagrams describing the relative content of mainly Si, Al, Ca, Fe, Mg, Na, K, Ti, Mn and P (NEA 2016). These chemical properties should in principle be well suited for an ERT/IP mapping approach, with the sulphides acting both as electronic conductors and polarizable particles. Whereas ERT has shown to correctly and repeatedly map black shales as very conducting bodies (resistivity down to 0.1 Ωm), IP measurements do more often give inconsistent results of poor quality (Bazin et al. 2015, Lysdahl et al. 2015).

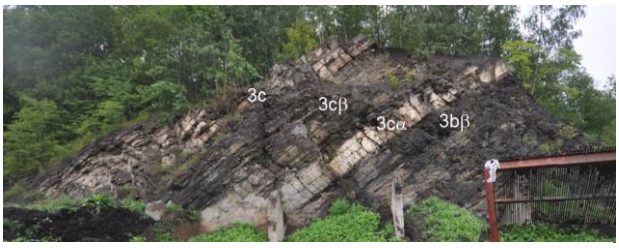

Figure 1. The sedimentary rocks at Slemmestad, Oslo graben: Galgeberg (3bβ) and Huk (3cα, 3cβ and 3c). Elnes (4a) further left is behind the vegetation and not visible on the photo.

METHOD

We have performed an ERT/IP field survey at a well-studied geologic profile at Slemmestad outside Oslo, and we have acquired complex impedance data from laboratory measurements on representative black shale samples from the same lithology at a different location in Oslo. The geologic profile at Slemmestad is well exposed and shown in Figure 1. From right (oldest rocks) to the left (youngest rocks), the sequence consists of the black shale Galgeberg (code 3bβ), the limestone Huk (3c) and the gray-black shale Elnes (4aα). Huk is divided in three parts, of which the middle is a softer, limestone-rich shale. The laboratory samples are taken from layer 2-3bβ in the same lithology. We installed the acquisition cable on top of the outcrop some 20 m from the cliff, perpendicular to the strike. We acquired the data with an ABEM Terrameter LS instrument using the Gradient-Plus array, and we used Res2DInv to invert the data. We used the apparatus "Chameleon" for the laboratory impedance measurements (Radic 2014).

RESULTS AND DISCUSSION

The resulting resistivity model (Figure 3, upper plot) is relatively easily interpreted and in accordance with the geology. The resistivity model shows the lithologic layers inclined approximately 30 degrees with the horizontal (indicated by dotted lines). Of these corresponds the two high-resistive (around 1000 Ωm) layers to the limestones 3cα and 3c whereas the limestone-rich shale in between (3cβ) shows lower values (around 200 Ωm). The black shale 3bβ (around 10 Ωm) is recognized below the limestone around profile meter 70. A layer of sediments is indicated left of the limestone and marked with a solid line. The rock below shows in general lower values, consistently with the known gray-black shale 4aα, but with some heterogeneity. The 3bβ-3cα boundary is the only one which is badly resolved and misplaced in the resistivity model.

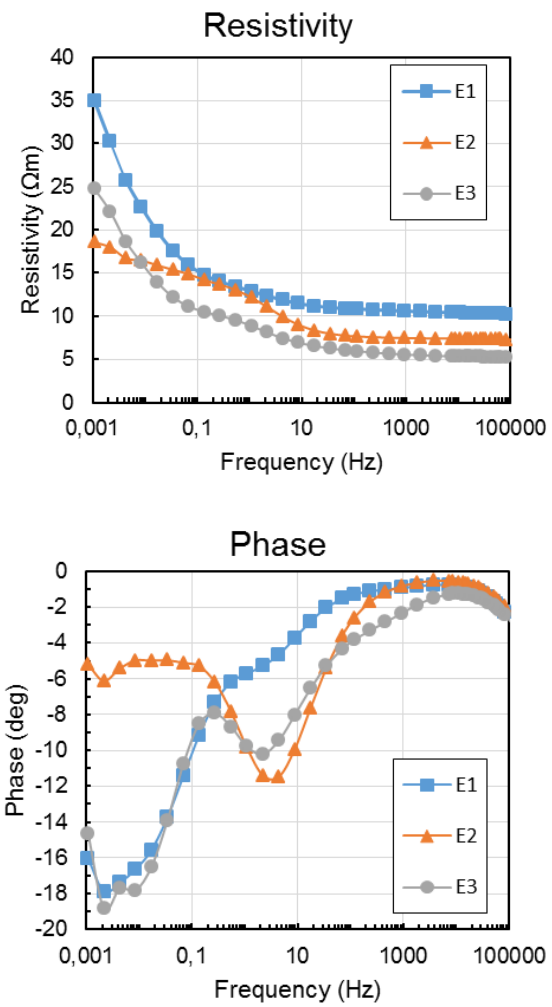

Figure 2. Complex resistivity measurement on three black shale samples E1, E2 and E3. Geochemical characterization is pending.

The time-domain IP inversion (Figure 3, lower plot) shows a smoothly varying distribution of the time constant (chargeability) which similarly corresponds well with the lithology. The black and gray shales on each side of the limestone stand clearly out with chargeability around 40 msec in contrast to limestone with low chargeability (around 5 msec). The 3bβ layer is actually better mapped than in the resistivity model. Even the sediment layer around profile 35 m and an outcrop registered around 25 m is identified. This is to the author's knowledge the first time Norwegian black shales have successfully been mapped in an IP field survey.

The resistivity model has in general a much higher resolution in the near-surface and is suitable for an accurate localization of the boundaries. However, the resistivity distribution shows large variations, especially in the leftmost part in the Elnes (4aα) area. This may be caused by differences in the shale geochemistry or anisotropy, but interestingly, the IP distribution is more homogeneous. However, the higher content of sulphides in 3bβ compared to 4aα (NEA 2016) cannot be observed in the IP distribution.

The complex impedance measurements are shown in Figure 2. All samples have resistivity around 5-15 Ωm (upper plot), which falls in the expected range for dark gray and black shales (i.e. Galgeberg 3bβ) (Lysdahl et al. 2015). E2 and E3 seem to have slightly higher content of electronic conducting sulphides. The low-frequency phase shift can qualitatively be compared to the time-domain chargeability, and looking at the phase spectrum (lower plot), especially E1 and E2 show a significant IP effect (up to 19 degrees phase shift) at low frequencies, which compares well with the field measurements. A first inspection of the samples has not revealed especially large mineral grains, but the effect may still occur if the sulphide minerals touch each other and form large polarizable aggregates. Such aggregates do not necessarily affect the electronic conductivity significantly. A geochemical analysis of the samples is soon to be carried out and will enable us to better understand the origin of the measured impedance and how geophysical measurements can be used to characterize black shales. The geochemical properties of all the shales in this lithology (layer 2-4a) are well studied and will justify a comparison. We will give a more complete discussion at the workshop when the geochemical analysis is at hand.

CONCLUSIONS

The time-domain IP field measurements show that gray and black shales Galgeberg (3bβ) and Elnes (4aα) have a high chargeability of around 40 msec, and the calculated inversion model gives a correct image of the known lithology. The frequency-domain complex impedance measurements supports the field data at low frequency especially in two of the three black shale samples, with a phase shift of up to 19 degrees. Both methods suggest the existence of large, polarizable minerals or aggregates in the black shales studied. A more detailed analysis of the relationship to the geochemical content is to come. In total, this suggests that IP is a good method to identify and also characterize black shales.

REFERENCES

Bazin, S. et al., 2015, On the Use of ERT and AEM Resistivities for a Tunnel Pre-investigation. EAGE European Airborne Electromagnetics Conference, Turin, Italy.

Lysdahl, A. K. et al., 2015, Black shale mapping by AEM for geotechnical applications. EAGE European Airborne Electromagnetics Conference, Turin, Italy.

Norwegian Environment Agency (NEA), 2016, Identifisering og karakterisering av syredannende bergarter. http://www.miljodirektoratet.no/Documents/publikasjoner/M310/M310.pdf

Radic, T., 2014, Measuring IP effects at high frequencies: First lab and field data from 0.001 Hz – 250 kHz. 3rd international workshop on Induced Polarization, Ile d'Oléron, Charente-Maritime, France.

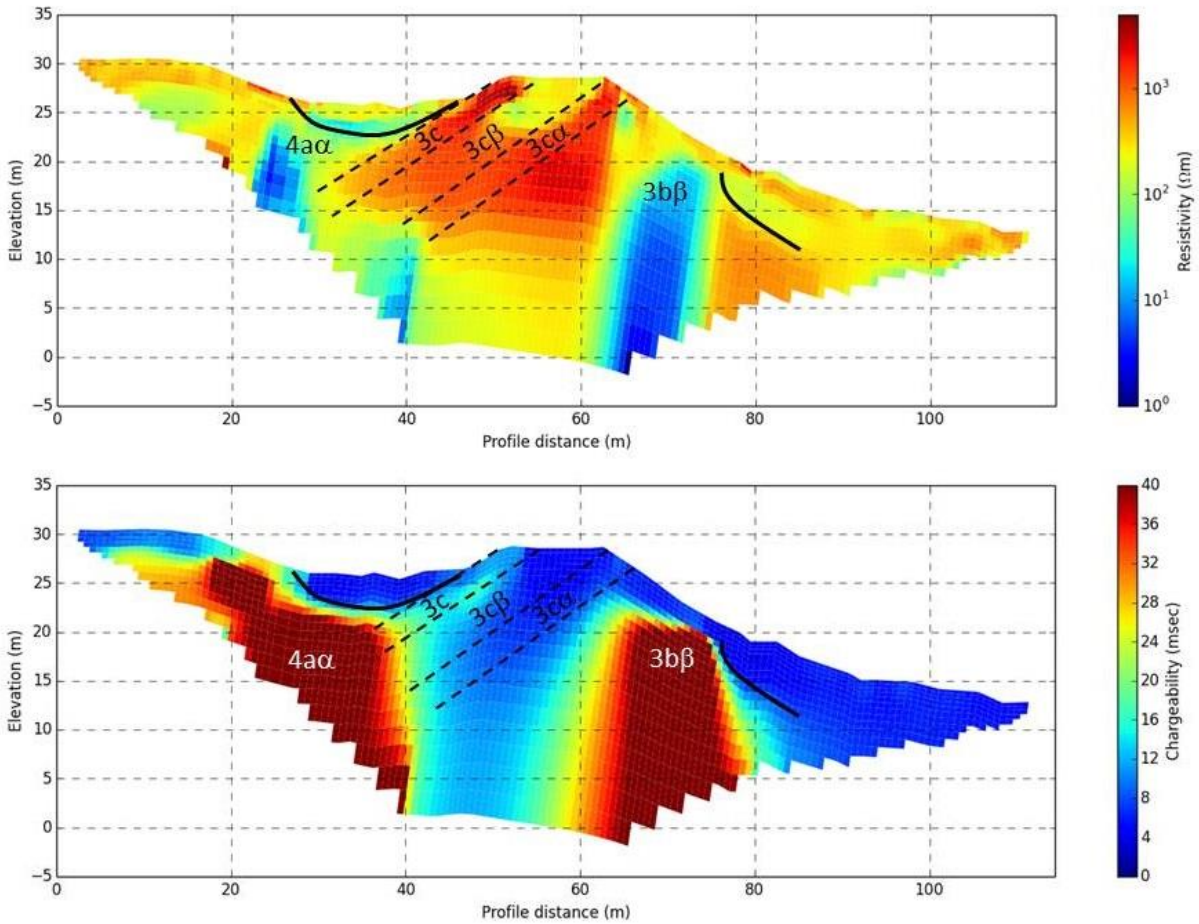

Figure 3. Resistivity (upper chart) and time-domain IP (lower chart) field measurements on the Slemmestad lithology.

IP2016 / 4th International Workshop on Induced Polarization

Bayesian inference of spectral induced polarization parameters at the Canadian Malartic disseminated gold deposit

Charles Lafrenière-Bérubé
École Polytechnique Montréal
2900 boul. Édouard-Montpetit,
Montréal, QC H3T 1J4
charles.lafreniere@polymtl.ca

Michel Chouteau
École Polytechnique Montréal
2900 boul. Édouard-Montpetit,
Montréal, QC H3T 1J4
michel.chouteau@polymtl.ca

Gema R. Olivo
Queen's University
99 University Ave,
Kingston, ON K7L 3N6
olivo@queensu.ca

SUMMARY

Spectral induced polarization (SIP) parameters can be extracted from field or laboratory complex resistivity measurements, and even airborne or ground frequency domain electromagnetic data. There is a growing interest in application of SIP to environmental problems and mineral exploration. SIP measurements were conducted on 211 rock samples from the Canadian Malartic disseminated gold deposit to study its electric signature that could be detected by geophysical prospecting. Then, the SIP parameters were inferred using Markov-chain Monte Carlo simulation with the Cole-Cole, Dias, Debye decomposition and Shin models. Meta-sedimentary rocks with a well-defined schistosity and pyrite alteration produce higher chargeability peaks than pyrite-poor or silicified samples. The characteristic relaxation time is also inversely related to the observable quantity of fine-grained (1 to 100 microns) pyrite per unit area. Meta-sedimentary rocks of Canadian Malartic with a pyrite content of 1 to 5% are commonly associated with gold contents above 1 ppm, and they produce a chargeability peak at short relaxation times (0.01 to 0.1 s). Non-mineralized rocks with fewer, larger pyrite grains produce a chargeability peak at longer relaxation times (0.1 to 10 s). Spectral induced polarization may be the key in defining the electric footprint of the Canadian Malartic and similar disseminated gold deposits, where high gold grades are associated with finely disseminated sulphides.

Key words: Spectral induced polarization (SIP), stochastic inversion, disseminated gold

INTRODUCTION

No specific electric or electromagnetic signature has yet been identified at the Canadian Malartic or similar disseminated gold deposits. Thus geophysical prospecting for this type of deposit in similar geological environments is poorly defined. Physical properties of the ore and host rock are dependent on their mineralogical composition and textures, which relates to their original composition, deformation, metamorphism, and fluid-rock interaction history. The aim of this study is to measure the physical properties of the various rock types from the core of the mineralized system to the outer zones of the Canadian Malartic gold deposit to help anticipate the signals that could be detected by geophysical surveys. Spectral induced polarization (SIP) measurements were done on 211 core and outcrop samples from the Canadian Malartic disseminated gold deposit, in order to study its electrical footprint.

The Canadian Malartic deposit is a world class, large tonnage and low-grade Archean gold deposit located in the Pontiac Province, Québec, Canada. It is situated in the proximity of the Cadillac-Larder Lake tectonic zone, south of the boundary between metamorphosed siliciclastic sedimentary rocks of the Pontiac Group and mafic to ultramafic volcanic and intrusive rocks of the Piché Group. The mineralization is hosted mainly (70%) in meta-sedimentary rocks (greywackes), partly in felsic to intermediate porphyry intrusions (monzodiorites), and rarely in mafic dykes. Gold occurs mainly as fine-grained native gold grains disseminated in the host rock, included in pyrite, or along the contacts between minerals such as pyrite, potassium-feldspar, plagioclase, biotite or quartz. Across the deposit, gold mineralization is associated with a halo of 1 to 5 % disseminated pyrite (Helt et al., 2014). In the 1980's, time-domain induced polarization surveys were conducted on a large part of the mining site. These surveys turned out to be inconclusive, and it is believed that the low amount (1 to 5%) of disseminated pyrite was insufficient to generate any induced polarization response.

Such small amounts of disseminated polarizable material in a porous media should generate an electrical response (Revil et al., 2015), and SIP parameters may help defining the ideal induced polarization survey parameters for prospecting similar deposits. Some ambiguity still exists in the meaning of SIP parameters such as relaxation time and chargeability. These parameters are related to the porosity and permeability of the rock (Zisser et al., 2010), and to metallic grain size and oxidation level (Gurin et al., 2013; Placiencia-Gomez et al., 2013). Several models have been proposed to fit frequency-domain induced polarization spectra and obtain these parameters. We developed an open-source Python module and standalone application to perform Bayesian inference of SIP parameters using the Debye decomposition approach, the Cole-Cole model, the Dias model, and the recently proposed model of Shin et al. (2015). Bayesian inference allows the estimation of a system's optimal parameters and their uncertainties (posterior distribution) from measurements and their errors (observations), and from knowledge about the parameters (prior distributions). The posterior distribution of SIP parameters is estimated using Markov-chain Monte Carlo (MCMC) simulation (Chen et al., 2008; Keery et al., 2012).

The SIP parameters, porosity, quantitative mineralogy, texture and whole-rock geochemistry of 12 rock samples from the Canadian Malartic gold deposit are reported and discussed in this contribution. It is observed that the frequency dependence and chargeability parameters of the Cole-Cole model are

related to the rocks sulfur content. Schistosity of the rock and pyrite grain orientation also influence the SIP response, and it is noted that the quantity of metallic grain per unit area is inversely related to the relaxation time parameter of all 4 models. Experimenting with the code shows that the Cole-Cole, Debye decomposition, and Shin models converge to a solution after 1 to 5 chains of 100 000 iterations (20 to 100 seconds computation time), and often provide the best fit with experimental data. The Dias model requires only a chain of 50 000 iterations to fully converge, but we note a small discrepancy between experimental data and analytical model for most samples.

METHODS

Prior to measurements, rock samples extracted from drill cores or outcrops are drilled and cut to obtain a cylindrical core with diameter of 2.5 cm and a length of 1 to 2 cm. Samples are then wrapped in nitrile rubber and liquid paraffin is poured around the core sample in a 3.75 cm diameter by 2 cm length cylindrical mould. Once the paraffin has set, excess paraffin and nitrile rubber are removed in order to expose two opposite faces of the sample. This procedure insures that the paraffin cannot infiltrate and contaminate the rock pore network, and that all samples fit in the sample holder, where the paraffin prevents any current from circulating around the rock. Samples are then left to soak at the bottom of a tank filled with a 28 to 32 Ohm-m tap water for 48 hours.

The sample holder used for spectral induced polarization measurements is a 4-point electrodes type sample holder. Two copper needles (A-B) are used to inject current from one water-filled cell to another, and two non-polarizable Ag-AgCl point-electrodes (M-N) are used to measure the voltage in the water on each side of the rock sample. The induced polarization spectra are acquired by measuring the phase shift and amplitude of complex resistivity at 17 frequencies ranging from 11.4 mHz to 750 Hz using the SIP Fuchs-III equipment from Radic Research, Germany.

One of the main advantages of using a stochastic approach to estimate the SIP parameters is that the influence of initial guesses for the parameters is decreased as the MCMC simulation progresses. This makes it ideal for batch inversion of complex resistivity spectra measured in laboratory by minimizing the amount of inputs from the user. In each model we choose uniform prior distributions for the parameters to be estimated. Lower and upper bounds of the prior distributions are given based on the physical meaning of the parameter (e.g. $0 < \text{chargeability} < 1$). At each step in the chains, random values for the parameters are selected or rejected based on the Metropolis algorithm implemented in the PyMC python module. The likelihood of the corresponding simulated spectra is computed using the assumption that errors are independent for the real and imaginary parts of resistivity, and that the errors on the measurements are random and follow a normal distribution (Ghorbani et al., 2007).

RESULTS

Phase response and Debye relaxation time distribution

The textural and mineralogical attributes of two greywackes from the Canadian Malartic gold deposit are presented in Figure 1. Both samples comprise biotite, plagioclase and quartz, but sample K389055 (Figure 1a) contains up to 1330 ppb Au and presents a more developed schistosity, higher pyrite content, and smaller pyrite grain distribution than sample K389058 (Figure 2).

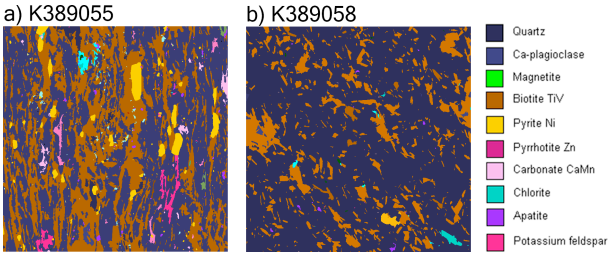

Figure 1. Mineral liberation analysis images of two rock samples from the Canadian Malartic gold deposit. The two meta-sedimentary rocks, K389055 (1330 ppb Au) and K389058 (34 ppb Au), show similar mineral assemblages of quartz, Ca-plagioclase, and biotite. However, the first one displays a strong schistosity, has gold mineralization, and is altered with albite, carbonates and pyrite. Pyrite grains are aligned with the schistosity, which is marked by the preferred orientation of biotite grains.

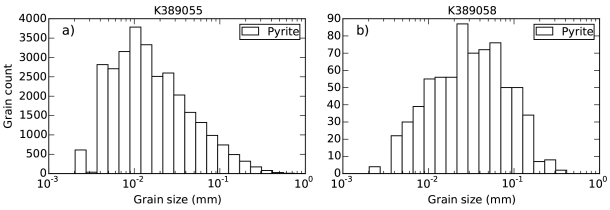

Figure 2. Grain size distribution of pyrite, the main sulphide mineral in samples K389055 (a) and K389058 (b). The first sample has a median pyrite grain size of 14 microns, and contains up to 1330 ppb Au and 3.57% pyrite. The second sample has a median grain size of 30 microns, and contains up to 34 ppb Au and 0.19% pyrite.

The complex resistivity spectra of both samples are also different. In the mineralized and foliated greywacke, the phase shift peak is observed in the 1 to 10 Hz range, while it is observed in the 0.1 to 1 Hz range for the unaltered sample (Figure 3). The high frequency response is visible on the phase spectra at frequencies above 100 Hz for the pyrite-rich rock, and frequencies above 10 Hz for the barren sample. For rock samples of similar mineral assemblage, the phase response is also higher for pyrite-rich rocks and generally lower in barren samples. Fitting the complex resistivity spectra of both rocks with the Debye decomposition approach produces the relaxation time distributions presented in Figure 4.

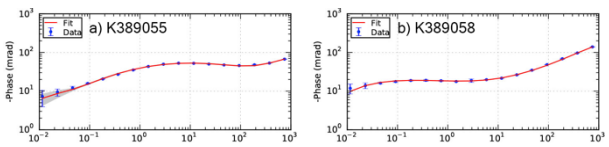

Figure 3. Phase spectra and fit with the Debye decomposition approach for rock samples (a) K389055, and (b) K389058. Both phase curves display the high-frequency response (> 100 Hz) associated with processes unrelated to the electrical double-layer. Sample K389055 has a phase peak of -53 mrad at a frequency of 5.86 Hz and sample K389058 has a phase peak of -19 mrad at 0.37 Hz. The optimal parameters produce a response that fits the data within the measurement uncertainty in both cases.

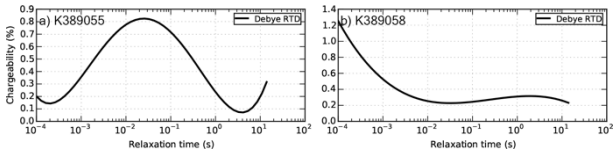

Figure 4. The complex resistivity spectra of samples K389055 and K389058 are fitted with a 4th and 3rd order polynomial Debye relaxation time distribution (RTD), respectively. The first sample has a maximum chargeability of 0.81% at a peak relaxation time of 0.02 second. The second sample has a maximum chargeability of 0.33% at a peak relaxation time of 2 seconds, when not considering the high-frequency response.

Relaxation time and pyrite grains per unit area

For all 12 samples with quantitative mineralogical information available, the characteristic relaxation time is inversely correlated to the amount of pyrite grains observed per unit area on polished thin section (Figure 5). This result is valid for the Cole-Cole, Debye, Dias and Shin models, and the relaxation times inferred using these models are correlated with each other. It is believed that rocks with high gold contents, which are associated with a large number of small pyrite grains (Figure 2), produce a chargeability peak at shorter relaxation times than the non-mineralized rocks with fewer, larger pyrite grains. Values for porosity, resistivity, magnetic susceptibility, density, chargeability, relaxation time, and pyrite content are also presented in Table 1.

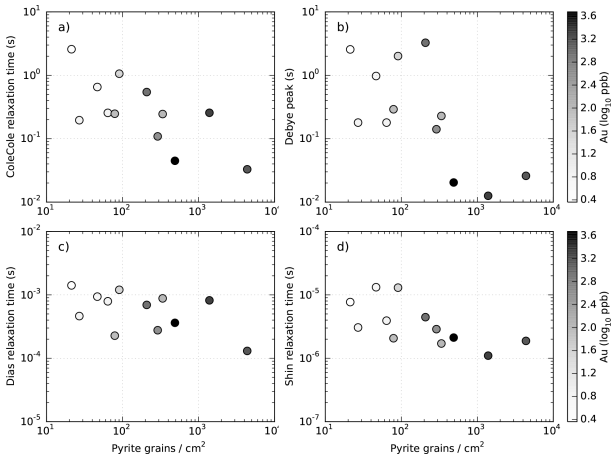

Figure 5. Relaxation times obtained by stochastic inversion on 12 rock samples from the Canadian Malartic gold deposit. The greyscale legend bar indicates the gold content of each sample. In the Cole-Cole model (a), rock samples with over 1000 ppb Au tend to possess a characteristic relaxation time that is lower than 0.1 second. The same observation is made when using the Debye decomposition approach and considering the peak relaxation time (b).

SIP parameters and total sulphide content

For the main lithology that hosts the Canadian Malartic gold deposit, the influence of total sulphur content on the SIP response is characterized by an increase of Cole-Cole chargeability (m) and frequency dependence (c). These two parameters are correlated when doing inversion of complex resistivity spectra. Consequently, as the MCMC simulation progresses, small increments (10^{-3} to 10^{-4}) of chargeability in the range 0.2 to 0.3 tend to be compensated by equally small decrements of frequency dependence in the same range. This correlation may lead to a lack of convergence, even for simulations using millions of iterations. One way to remove this correlation is to fix the frequency dependence parameter to a certain value (e.g. 0.25, 0.5). Fixing this parameter, however, significantly reduces the quality of the fit (similar to the Dias model). Another way to avoid it is to consider a combination of both parameters (e.g. c + m, or the average between the two). Using this combination, we find that both frequency dependence and chargeability are related to total sulphur content (Figure 6) determined by infrared combustion (LECO ±0.005 %). The relaxation time values are correlated from one model to another, but only the Dias, Debye, and Shin definitions of chargeability are correlated. The Cole-Cole chargeability becomes correlated with the three other models only when the frequency dependence parameter is fixed.

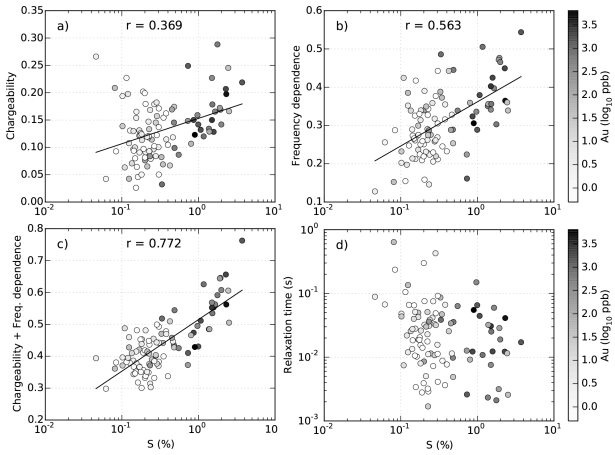

Figure 6. Correlations between sulphur content and Cole-Cole chargeability (a), frequency dependence (b), and the addition of both parameters (c). The relaxation time parameter does not appear related to the total sulphur content (d). Only meta-sedimentary rocks of the Canadian Malartic gold deposit are considered.

CONCLUSIONS

Previous time-domain induced polarization work has failed to identify any chargeability or resistivity anomalies at the Canadian Malartic gold deposit. However, the analysis of rock complex resistivity spectra measured in the laboratory shows that pyritic alteration in high-schistosity meta-sedimentary rocks produces chargeability peaks at shorter relaxation times than non-mineralized rocks. Contrary to what might be expected, no direct link between chargeability and pyrite content is observed. However, we find a relationship with total sulphur content when considering both the chargeability and frequency dependence parameters of the Cole-Cole model. It is also important to note that some of the most altered and pyrite-rich samples are silicified, which may fill the pore connectivity, reduce porosity and therefore attenuate the SIP response. The results presented here are in agreement with the principle that smaller polarizable particles are associated with shorter relaxation times. Spectral induced polarization may be the key to defining the electric footprint of the Canadian Malartic and similar disseminated gold deposits. When gold is present as inclusions in microscopic pyrite grains, the induced polarization response is maximal between frequencies of 1 to 10 Hz. Additional SIP measurements and stochastic inversions will be conducted on a more extensive collection of samples from the Canadian Malartic gold deposit, the Highland Valley porphyry-copper deposit, and the Millennium-McArthur uranium deposits.

ACKNOWLEDGMENTS

Thanks to S. Perrouty, N. Gaillard, P. Lypaczewski, N. Blacklock, T. Raskevicius, R. Mir, R. Thiémonge, and G. Gauthier for helping with sampling and fieldwork. Thanks to François Bouchard and the Canadian Malartic Mine. Research funded by Canada Mining Innovation Council (CMIC) and NSERC CRD Program. CMIC-NSERC Exploration Footprints Network Contribution 082.

REFERENCES

Chen, J., Kemna, A., and Hubbard, S. S. (2008). A comparison between Gauss-Newton and Markov-chain Monte Carlo–based methods for inverting spectral induced-polarization data for Cole-Cole parameters. Geophysics, 73(6): F247–F259.

Ghorbani, A., Camerlynck, C., Florsch, N., Cosenza, P., and Revil, A. (2007). Bayesian inference of the Cole–Cole parameters from time- and frequency-domain induced polarization. Geophysical Prospecting, 55(4): 589–605.

Gurin, G., Tarasov, A., Ilyin, Y., and Titov, K. (2013). Time domain spectral induced polarization of disseminated electronic conductors : Laboratory data analysis through the Debye decomposition approach. Journal of Applied Geophysics, 98: 44–53.

Keery, J., Binley, A., Elshenawy, A., and Clifford, J. (2012). Markov-chain Monte Carlo estimation of distributed Debye relaxations in spectral induced polarization. Geophysics, 77(2): E159–E170.

Placencia-Gomez, E., Slater, L., Ntarlagiannis, D., and Binley, A. (2013). Laboratory SIP signatures associated with oxidation of disseminated metal sulfides. Journal of Contaminant Hydrology, 148: 25–38.

Revil, A., Florsch, N. and Mao, D. (2015). Induced Polarization Response of Porous Media with Metallic Particles — Part 1: A Theory for Disseminated Semiconductors. Geophysics, 80(5): D525–38.

Shin, S. W., Park, S., and Shin, D. B. (2015). Development of a New Equivalent Circuit Model for Spectral Induced Polarization Data Analysis of Ore Samples. Environmental Earth Sciences 74(7): 5711–16.

Zisser, N., Kemna, A., and Nover, G. (2010). Relationship between low-frequency electrical properties and hydraulic permeability of low-permeability sandstones. Geophysics, 75(3): E131–E141.

Sample ID	Au (ppb)	Pyrite (%)	Mag susc (SI)	Density (g/cc)	Porosity (%)	Resistivity (Ohm-m)	ColeCole m	ColeCole tau (s)	ColeCole c	Debye m	Debye Peak (s)	Dias m	Dias tau (s)	Shin m	Shin tau (s)
K389005	395	0.95	2.94E-04	2.767	0.161	5.37E+03	0.102	1.09E-01	0.407	0.112	1.41E-01	0.151	2.77E-04	0.098	2.88E-06
K389019	1840	2.73	1.22E-04	2.759	0.296	5.35E+03	0.027	2.56E-01	0.630	0.251	1.26E-02	0.253	8.20E-04	0.169	1.10E-06
K389046	5.2	0.17	4.50E-05	2.751	0.092	1.22E+04	0.145	6.53E-01	0.505	0.304	9.74E-01	0.322	9.38E-04	0.216	1.32E-05
K389055	1330	3.57	2.19E-04	2.827	0.259	4.90E+03	0.197	3.29E-02	0.537	0.216	2.60E-02	0.323	1.31E-04	0.199	1.88E-06
K389058	34	0.19	4.83E-04	2.743	0.03	6.01E+03	0.111	1.06E+00	0.369	0.203	2.01E+00	0.268	1.20E-03	0.193	1.30E-05
K389062	7.4	0.35	1.98E-02	2.762	0.14	5.03E+03	0.098	2.56E-01	0.422	0.199	1.79E-01	0.211	7.92E-04	0.169	3.92E-06
K389077	2.3	0.01	1.34E-03	3.066	0.219	2.97E+04	0.057	2.58E+00	0.318	0.088	2.56E+00	0.156	1.41E-03	0.113	7.70E-06
K389198	93.1	0.70	7.50E-05	2.703	0.288	8.97E+03	0.052	2.45E-01	0.471	0.137	2.28E-01	0.148	8.80E-04	0.114	1.71E-06
K389214	6.3	0.22	2.71E-04	2.735	0.118	9.30E+04	0.114	1.96E-01	0.540	0.227	1.79E-01	0.246	4.63E-04	0.186	3.06E-06
K389216	833	0.35	4.22E-04	2.762	0.117	2.34E+04	0.065	5.44E-01	0.268	0.067	3.26E+00	0.132	6.95E-04	0.064	4.45E-06
K389219	4720	1.79	2.54E-04	2.776	0.156	8.00E+03	0.079	4.48E-02	0.311	0.072	2.04E-02	0.113	3.62E-04	0.084	2.12E-06
K389227	87.8	1.26	7.83E-03	2.711	0.205	1.31E+04	0.156	2.48E-01	0.461	0.181	2.91E-01	0.215	2.27E-04	0.151	2.07E-06

Table 1. Gold and pyrite contents, magnetic susceptibility, density, porosity, resistivity and spectral induced polarization parameters of 12 rock samples from the Canadian Malartic gold deposit.